

The rotational and magnetic properties of Polaris from long-term spectropolarimetric monitoring

JAMES A. BARRON ¹, GREGG A. WADE ², AND COLIN P. FOLSOM ³

¹*Department of Physics, Engineering Physics & Astronomy, Queen's University, 64 Bader Lane, Kingston, ON K7L 3N6, Canada*

²*Department of Physics & Space Science, Royal Military College of Canada, P.O. Box 17000, Station Forces, Kingston, ON K7K 7B4, Canada*

³*Tartu Observatory, University of Tartu, Observatooriumi 1, Tõravere, 61602, Estonia*

(Received March 10, 2025)

Submitted to AAS Journals

ABSTRACT

Polaris is a highly unusual Cepheid with observed properties that are difficult to reconcile with stellar evolutionary models. Since the initial detection of Polaris' magnetic field in 2020, we have conducted a magnetic monitoring campaign with the ESPaDOnS spectropolarimeter at the Canada-France-Hawaii Telescope. We compute Stokes V least-squares deconvolution profiles and measure the associated mean longitudinal magnetic field strengths $\langle B_z \rangle$. The surface magnetic field has remained remarkably stable over five years of observations, with $\langle B_z \rangle$ varying between approximately -3 G and $+0.6$ G. From the periodic modulation of $\langle B_z \rangle$ we infer a stellar rotation period of $P_{\text{rot}} = 100.29 \pm 0.19$ days. This is the first direct measurement of P_{rot} for a classical Cepheid. Previous interferometric radius measurements and P_{rot} imply an equatorial rotation velocity of $v_{\text{eq}} = 23.3 \pm 0.2$ km s⁻¹. We set a conservative upper bound on the projected equatorial rotational velocity of $v_{\text{eq}} \sin i_{\star} < 13.5$ km s⁻¹ and constrain the stellar inclination angle to be $i_{\star} < 37^{\circ}$. Using the previously determined orbital solution, we find a high likelihood of a strong spin-orbit misalignment. We determine the lower bound on the obliquity angle between the stellar rotation and orbital axes to be $\beta > 18.7^{\circ}$ at 99% confidence. We discuss the challenges in interpreting the origin and properties of the surface magnetic field in the context of Polaris' uncertain evolutionary history and the merger hypothesis.

Keywords: Cepheid variable stars (218) — Stellar magnetic fields (160) — Starlight polarization (1571)
— Stellar rotation (1629) — Stellar astronomy (1583)

1. INTRODUCTION

As the pole star, Polaris (α UMi, HD 8890) is one of the best known stars in the night sky. It is the nearest and brightest classical Cepheid (hereafter Cepheid), and has been the subject of extensive study since the mid 1800's (e.g. L. Seidel 1852; W. W. Campbell 1899; E. Hertzsprung 1911; E. Roemer 1965; A. Arellano Ferro 1983; D. G. Turner et al. 2005; R. I. Anderson 2019; G. Torres 2023). Keen interest in Polaris has been driven by puzzling changes in its variability and challenges in reconciling its inferred physical properties with stellar pulsation and evolution models.

J. A. Barron et al. (2022) reported the first high-resolution, circularly polarized spectroscopic observation of Polaris as part of first results from a large magnetic survey of Cepheids. A Stokes V Zeeman magnetic signature was detected at high signal-to-noise ratio (S/N), with a corresponding weak mean longitudinal magnetic field measured with sub-gauss precision. It is becoming clear that Cepheid surface magnetic fields are frequently detectable in (ultra)-high S/N spectropolarimetric observations (J. H. Grunhut et al. 2010; J. A. Barron et al. 2022, 2024, in prep.). However, we know little about the origins of these fields and their relation to pulsation dynamics.

We have conducted a long-term spectropolarimetric monitoring campaign of Polaris using the Echelle SpectroPolarimetric Device for the Observation of Stars (ESPaDOnS) at the Canada-France-Hawaii-Telescope

(CFHT). Polaris is an ideal Cepheid target for magnetic monitoring due to its bright apparent magnitude, which permits high-precision magnetic measurements to be acquired in reasonable integration times. Additionally, Polaris’ Stokes V profiles show less distortion and appear easier to interpret compared to Cepheids such as δ Cep or η Aql (J. A. Barron et al. 2022).

In stars with non-axisymmetric magnetic fields, the Zeeman induced Stokes V signatures and corresponding $\langle B_z \rangle$ measurements are periodically modulated by the stellar rotation as different regions of the star’s magnetic geography are seen by the observer (J.-F. Donati & J. D. Landstreet 2009). This makes stellar magnetometry an effective method to directly measure rotation periods, particularly in slowly rotating stars that do not present unambiguous rotationally modulated signals in spectral or photometric time-series (e.g. Cepheids).

Rotation is a fundamental stellar property, impacting evolutionary tracks and surface chemical abundances (G. Meynet & A. Maeder 2000; S. Ekström et al. 2012). Cepheid blue-loops are sensitive to the initial rotation rate at the zero-age main-sequence (ZAMS), suggesting that rotation is a key ingredient in resolving the long-standing Cepheid mass-discrepancy problem (R. I. Anderson et al. 2014, 2016; L. Zhao et al. 2023). Furthermore, rotation and magnetic field evolution are interconnected processes. Rotation is essential for the generation of both convective and radiative dynamos (P. J. Käpylä et al. 2023 and references therein). In turn, coupling between the magnetic field and stellar wind leads to angular momentum loss and stellar spindown (E. J. Weber & L. Davis 1967; A. ud-Doula et al. 2009).

Recent results necessitate a direct measurement of Polaris’ rotation period. An apparent age discrepancy between the Cepheid Polaris Aa and its distant companion Polaris B has led to the suggestion that the Cepheid may be a merger product (H. E. Bond et al. 2018; N. R. Evans et al. 2018; R. I. Anderson 2018). This is an intriguing possibility, considering the growing evidence that mergers are a viable channel to produce strong magnetic fields in intermediate and massive stars (F. R. N. Schneider et al. 2016, 2019; D. Korčáková et al. 2022; T. Shenar et al. 2023; A. J. Frost et al. 2024; D. Korčáková et al. 2025; F. R. N. Schneider 2025). A constraint on Polaris’ rotation rate at the ZAMS in concert with recent interferometric radius and dynamical mass measurements (N. R. Evans et al. 2024) will permit detailed comparison to evolution models and testing of the merger hypothesis.

N. R. Evans et al. (2024) reported the detection of surface spots on Polaris from an interferometric surface image reconstruction using the CHARA Array. The na-

ture of these surface features and their possible relation to the magnetic field geometry is unclear. Relatedly, there is ambiguity surrounding the origin and stability of Polaris’ long spectral periods ($\gtrsim 40$ days; H. Bruntt et al. 2008; R. I. Anderson 2019; K. Barbey et al. 2025), which may be due to rotating surface features (N. Dinshaw et al. 1989; B.-C. Lee et al. 2008) or non-radial pulsations (A. P. Hatzes & W. D. Cochran 2000).

In this paper, we present results from five years of spectropolarimetric monitoring of Polaris. In Sec. 2 we summarize Polaris’ physical and variability properties, in Sec. 3 we discuss the ESPaDOnS observations and in Sec. 4 we present the magnetic analysis. In Sec. 5 we perform a variability analysis on the RV and $\langle B_z \rangle$ measurements and determine the stellar rotation period. In Sec. 6 we determine broadening parameters from spectral fitting and constrain the stellar inclination angle. In Sec. 7 we constrain the spin-orbit misalignment of the inner binary Polaris Aa. In Sec. 8 we discuss our results, and in Sec. 9 we list our conclusions.

2. POLARIS

Polaris Aa (F8Ib, $\langle V \rangle = 2.0$ mag) the Cepheid is a member of a confirmed triple system. The inner single-lined spectroscopic binary consists of Polaris Aa in a ~ 30 year eccentric orbit (G. Torres 2023 and references therein) with Polaris Ab (F6 V; N. R. Evans et al. 2008). Separated at $\sim 18''$, Polaris B is a wide, gravitationally bound visual companion of spectral type \sim F3 V (N. R. Evans et al. 2008; I. A. Usenko & V. G. Klochkova 2008).

Polaris has a pulsation period of $P_{\text{puls}} \approx 3.97$ days, and shows remarkably low-amplitude, sinusoidal variations in radial-velocity (RV) measurements and photometry. More than a century of spectroscopic and photometric monitoring has revealed seemingly irregular changes in the pulsation period and amplitude over long time scales (e.g. G. Torres 2023). Proposed origins for this behaviour include magneto-convective cycles (R. B. Stothers 2009), pulsation instabilities (N. R. Evans et al. 2002) or tidal perturbations induced by the binary companion at periastron (G. Torres 2023).

Polaris’ pulsation mode and instability strip (IS) crossing number have been the subjects of vigorous debate (H. R. Neilson et al. 2012; D. G. Turner et al. 2013; H. R. Neilson 2014; Y. A. Fadeyev 2015; H. E. Bond et al. 2018; R. I. Anderson 2018; N. R. Evans et al. 2018, 2024). The conflicting interpretations are largely due to disagreement about Polaris’ distance before *Gaia* (S. G. Engle et al. 2018). N. R. Evans et al. (2024) adopt a *Gaia* DR3 distance of 136.90 ± 0.34 pc to the Polaris system, anchored to Polaris B. This value is close to the *Hipparcos* distance of 132.6 ± 1.9 pc for Polaris A

(F. van Leeuwen 2007, 2013). At this distance Polaris is considered a first overtone Cepheid from comparison to the period-luminosity and period-radius relations for fundamental Cepheids (M. W. Feast & R. M. Catchpole 1997; H. R. Neilson 2014; N. R. Evans et al. 2018). A first overtone pulsation mode is also supported by Fourier analysis of the RV curve, which is independent of the distance measurement (V. Hocdé et al. 2024).

The most recent spectroscopic studies of Polaris report an effective temperature $T_{\text{eff}} \approx 6000$ K and surface gravity $\log g \approx 2.0$ (I. A. Usenko et al. 2005; V. Ripepi et al. 2021). N. R. Evans et al. (2024) report a dynamical mass measurement of $M_{\star} = 5.13 \pm 0.28 M_{\odot}$ and a mean interferometric radius of $\langle R_{\star} \rangle = 46.27 \pm 0.42 R_{\odot}$.

Polaris A is a soft X-ray source with a luminosity ($\log L_X \approx 28.9 \text{ erg s}^{-1}$) and spectrum that could be produced by either Polaris Aa or Ab (N. R. Evans et al. 2010; S. Engle 2015; N. R. Evans et al. 2022). Polaris A’s X-ray flux does not show phase dependant enhancement seen in the higher amplitude Cepheids δ Cep and β Dor (S. Engle 2015; N. R. Evans et al. 2022). A circumstellar envelope (CSE) of unclear origin has been detected at $\sim 2.4 R_{\star}$, comprising $\sim 1.5\%$ of Polaris’ K -band flux (A. Mérand et al. 2006). As the temperature at this distance is too hot for dust formation, the CSE is may be due to free-free emission from an ionized gas shell (V. Hocdé et al. 2020).

3. OBSERVATIONS

We obtained spectropolarimetric observations of Polaris with ESPaDOnS at CFHT (J.-F. Donati et al. 2006). The observations were acquired between November 2020 and December 2025 under program IDs 20BC20, 21BC39, 22AC07, 22BC17, 23AC11, 23BC25, 24BC27 and 25BD03 (PI: Barron). ESPaDOnS is a bench-mounted, cross-dispersed echelle spectrograph with a spectral range of 370 – 1050 nm and a resolving power of $R \sim 65,000$. Each spectropolarimetric sequence consists of four sub-exposures between which the Fresnel rhombs are rotated in the Cassegrain-mounted polarimeter. The sequences were reduced using the Upena pipeline (based on Libre-ESPRIT; J. F. Donati et al. 1997) to produce one unpolarized Stokes I spectrum, one circularly polarized Stokes V spectrum and two diagnostic null spectra.

Multiple short-exposure sequences were obtained and co-added as Polaris quickly saturates the charge-coupled device due to its bright apparent magnitude. We excluded poor quality polarimetric sequences that were affected by poor observing conditions or technical issues, leaving 42 co-added observations for analysis. The spectra were combined and rectified using `normPlot` from

the `SpecpolFlow` software package (C. P. Folsom et al. 2025). The total integration time of the co-added spectra was reduced from ~ 2500 s for the 2020 observation to ~ 500 s for subsequent observations. The median S/N of all 42 co-added spectra is ~ 3000 at 500 nm (per 1.8 km s^{-1} pixel). Table A1 provides a log of all co-added observations.

4. MAGNETIC ANALYSIS

We performed a magnetic analysis similar to that described by J. A. Barron et al. (2022). We used the `SpecpolFlow` software package (C. P. Folsom et al. 2025) to generate least-squares-deconvolution (LSD) profiles (J. F. Donati et al. 1997; O. Kochukhov et al. 2010). The LSD profiles were computed with a velocity binning of 1.8 km s^{-1} using the tailored line mask generated by J. A. Barron et al. (2022) from 400 nm to 900 nm. The adopted LSD normalization parameters are $\lambda_0 = 500$ nm, $g_0 = 1.2$ and $d_0 = 0.1$ for the wavelength, effective Landé factor and line depth respectively. All LSD Stokes V profiles are definitely detected using the false alarm probability (FAP) metric and thresholds described by J. F. Donati et al. (1992, 1997). No spurious signatures are detected in the LSD N profiles. J. A. Barron et al. (2022) previously ruled out instrumental cross-talk from linear polarization as a contributor to Polaris’ Stokes V signatures.

We measured the centre-of-gravity radial velocity (RV_{cog}) of each LSD Stokes I profile using the first-moment method as implemented in `SpecpolFlow`. Each LSD profile was shifted by the corresponding RV_{cog} to correct for pulsation and orbital motion. The mean longitudinal magnetic field $\langle B_z \rangle$ for each observation was calculated from the first moment of the LSD Stokes V profile (J. F. Donati et al. 1997; G. A. Wade et al. 2000) using

$$\langle B_z \rangle = -2.14 \times 10^{11} \frac{\int vV(v)dv}{\lambda_0 g_0 c \int [1 - I(v)]dv} \quad (1)$$

where c is the speed of light and $I(v)$ and $V(v)$ are the continuum normalized Stokes I and V profiles. The $\langle B_z \rangle$ calculations were performed using constant integration bounds between -30 km s^{-1} and $+30 \text{ km s}^{-1}$ on the RV_{cog} corrected LSD profiles with `SpecpolFlow`. We find that $\langle B_z \rangle$ varies between approximately -3 G and $+0.6$ G with a typical uncertainties of ~ 0.3 G. The RV_{cog} and $\langle B_z \rangle$ measurements are reported in Table A1.

We re-measured $\langle B_z \rangle = 0.28 \pm 0.13$ G for the 2020 observation compared to $\langle B_z \rangle = 0.59 \pm 0.16$ G reported by J. A. Barron et al. (2022). This difference is primarily due to our adoption of a slightly smaller integration range and the exclusion of a single poor quality spec-

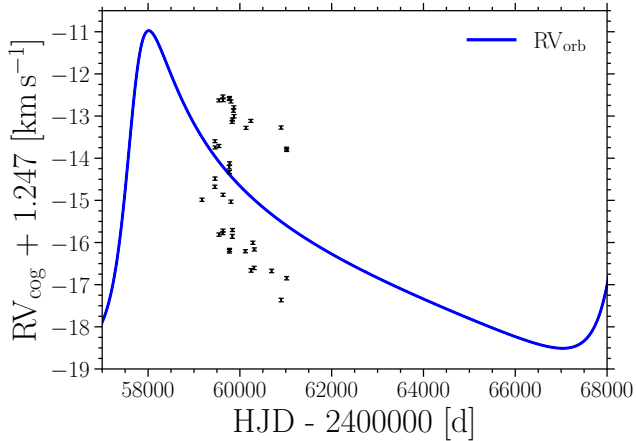


Figure 1. Offset corrected RV_{cog} measurements (black markers) shown in relation to the best fit orbital RV curve (solid blue line) given by N. R. Evans et al. (2024). The scatter in RV_{cog} is due to pulsation.

tropolarimetric sequence from the co-added observation.

5. VARIABILITY ANALYSIS

5.1. Pulsation Period and Amplitude

Figure 1 shows the RV_{cog} measurements in relation to orbital RV curve (RV_{orb}). We subtracted the systemic velocity and orbital motion from the RV_{cog} measurements using the “replicated” weighted orbital solution determined by N. R. Evans et al. (2024). After subtraction an offset of approximately -1.25 km s^{-1} remained as N. R. Evans et al. (2024) calibrated the zero-points of different RV data sets against the data presented by E. Roemer (1965).

We modelled the orbit-subtracted RV_{cog} measurements with a first-order sine function of the form

$$RV_{\text{cog}} - RV_{\text{orb}} = C + A \sin\left(\frac{2\pi}{P_{\text{puls}}}(t - t_0)\right) \quad (2)$$

where C is the systematic offset from the reference frame of the orbital solution and A is the semi-amplitude. We chose the reference epoch t_0 to coincide with the time of minimum radius nearest the middle of the observation span. This sets the pulsation phase $\phi_{\text{puls}} = 0$ to correspond to a pulsation-averaged velocity of 0 km s^{-1} on the descending branch of the pulsation curve. We determined best fit values and uncertainties for parameters in Eq. 2 using a Markov Chain Monte Carlo (MCMC) analysis described in Appendix B. We also experimented with fitting a two harmonic Fourier model similar to R. I. Anderson et al. (2024). However, we found that the inclusion of additional terms did not significantly alter the best fit model.

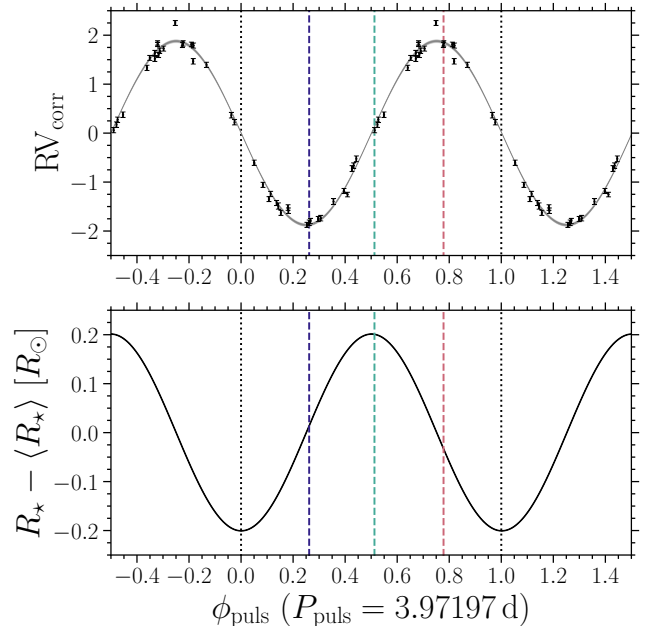


Figure 2. Top: Orbit and offset corrected RV measurements shown over two pulsation cycles. The grey lines show 100 random samples drawn from the MCMC joint posterior distribution. **Bottom:** Variation in radius inferred from the best fit pulsation model. The black dotted lines correspond to R_{min} and the dashed coloured lines correspond to the LSD profiles shown in Fig. 6.

We determined $P_{\text{puls}} = 3.97197(4)$ days, which is consistent with $P_{\text{puls}} = 3.972013(13)$ days reported by R. I. Anderson et al. (2024). The pulsation ephemeris over our observation span is

$$\text{HJD} = 2460095.714_{-0.005}^{+0.005} + 3.97197_{-0.00004}^{+0.00004} \cdot E \quad (3)$$

We determined an unsigned semi-amplitude of $|A| = 1.87 \pm 0.01 \text{ km s}^{-1}$ and offset $C = -1.247 \pm 0.008 \text{ km s}^{-1}$. We define the orbit- and offset-corrected RV measurements to be $RV_{\text{corr}} = RV_{\text{cog}} - RV_{\text{orb}} + 1.247$. Figure 2 shows RV_{corr} and the best fit model as a function of ϕ_{puls} . Values of RV_{corr} and ϕ_{puls} are recorded in Table A1.

The RV amplitude is largely consistent with measurements reported since 2020 (R. Buecke 2021; G. Torres 2023; I. A. Usenko et al. 2024), and the longer increasing trend observed since 1990 when the peak-to-peak amplitude reached a minimum of $\sim 1.5 \text{ km s}^{-1}$. However, the current pulsation amplitude remains low, even for an overtone Cepheid (R. I. Anderson et al. 2024).

The stellar radius as a function of time is calculated from

$$R(t) = \langle R_{\star} \rangle - p \int RV_{\text{corr}}(t) dt \quad (4)$$

where p is the projection factor (J. Storm et al. 2011). Polaris’ full amplitude of radius variation $\Delta R = R_{\max} - R_{\min}$ was determined by P. Moskalik & N. A. Gorynya (2005) to be $\Delta R \approx 0.17 R_{\odot}$. As the pulsation amplitude has increased over the past 20 years, we calculated a revised estimate of $\Delta R \approx 0.4 R_{\odot}$ from integration of the best fit RV_{corr} model. We adopted $p = 1.36$ to facilitate direct comparison with P. Moskalik & N. A. Gorynya (2005). The lower panel of Fig. 2 shows the radius variation as a function of ϕ_{puls} .

While Cepheid p -factors can range over $\sim 1.1 - 1.5$, precise determinations are challenging as p does not have a clear correlation with P_{puls} and other stellar parameters (B. Trahin et al. 2021). Our primary purpose for calculating ΔR is to obtain an order of magnitude estimate for the change in magnetic field strength due to the pulsation (Sec. 5.4). This estimation is not sensitive to our choice of p .

5.2. Rotation Period

The critical stellar rotation velocity is given by

$$v_{\text{crit}} = \sqrt{\frac{2}{3} \frac{GM_{\star}}{R_{\text{p,crit}}}} \quad (5)$$

where $R_{\text{p,crit}}$ is the polar radius at v_{crit} (S. Ekström et al. 2008). Adopting $R_{\text{p,crit}} = \langle R_{\star} \rangle$ (N. R. Evans et al. 2024) gives $v_{\text{crit}} \approx 120 \text{ km s}^{-1}$. The estimate of v_{crit} sets a conservative minimum stellar rotation period of $P_{\text{rot}}^{\min} \approx 20$ days.

We searched for significant periods above P_{rot}^{\min} in the $\langle B_z \rangle$ measurements using the generalized Lomb-Scargle (GLS) periodogram (N. R. Lomb 1976; J. D. Scargle 1982; M. Zechmeister & M. Kürster 2009; J. T. VanderPlas 2018). The GLS and window power were computed using the `LombScargle` class in the `astropy` Python package (Astropy Collaboration et al. 2022), and the FAP levels were estimated using the R. V. Baluev (2008) approximation. Figure 3 shows the GLS periodogram and window power. The highest peak at ~ 100.3 days and a peak at ~ 84.8 days are detected with $\text{FAP} < 0.001$. An additional period at ~ 49.1 days is detected with $\text{FAP} < 0.01$. From the analysis described in Sec. 5.3 we determined ~ 100.3 days to be the rotation period P_{rot} , and peaks at 84.8 days and 49.1 days to be aliases due to the time sampling of the variation. Significant peaks clustered near 1 day are due to the daily alias. The $\langle B_z \rangle$ measurements are well modelled by a first-order cosine function of the form

$$\langle B_z \rangle = B_0 + B_1 \cos\left(\frac{2\pi}{P_{\text{rot}}}(t - t_0)\right) \quad (6)$$

where B_0 is the mean of the $\langle B_z \rangle$ variation and B_1 is the semi-amplitude. We chose t_0 to correspond to the

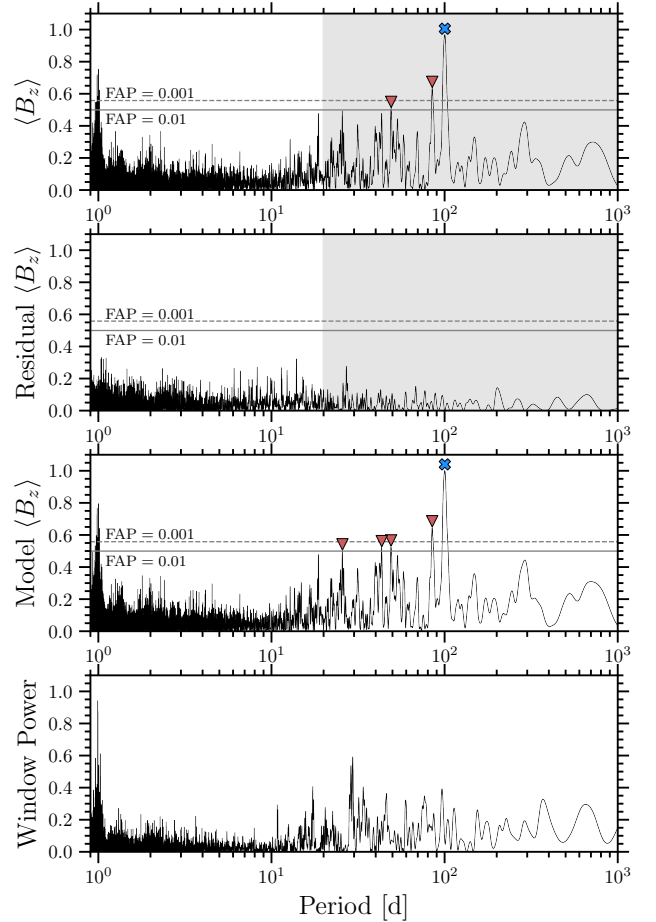


Figure 3. From top to bottom: GLS periodogram of $\langle B_z \rangle$ measurements, GLS periodogram of $\langle B_z \rangle$ residuals after subtraction of best fitting model, GLS periodogram of model $\langle B_z \rangle$ curve and window power spectrum. The solid and dashed grey lines denote the 0.01 and 0.001 FAP levels respectively. The blue ‘X’ denotes P_{rot} and red triangles denote long period aliases. Grey shaded regions indicate allowed rotation periods above P_{rot}^{\min} .

epoch nearest the middle of the observing span where $\langle B_z \rangle$ is maximum. Under this formulation the rotation phase $\phi_{\text{rot}} = 0$ corresponds to maximum $\langle B_z \rangle$.

To estimate robust parameter uncertainties, we fit Eq. 6 to the $\langle B_z \rangle$ measurements using a MCMC analysis described in Appendix B. We obtained $P_{\text{rot}} = 100.29 \pm 0.19$ days, $B_0 = -1.15 \pm 0.06$ G and $B_1 = 1.52 \pm 0.06$ G. The rotation ephemeris given by

$$\text{HJD} = 2460079.59_{-0.83}^{+0.83} + 100.29_{-0.19}^{+0.19} \cdot E \quad (7)$$

Table A1 provides ϕ_{rot} and rotation cycle number N_{rot} calculated from Eq. 7 for each observation. Figure 4 shows the $\langle B_z \rangle$ measurements as a function of observation date and phased to Eq 7. Figure 5 shows the LSD Stokes I , V and N profiles phased to Eq 7.

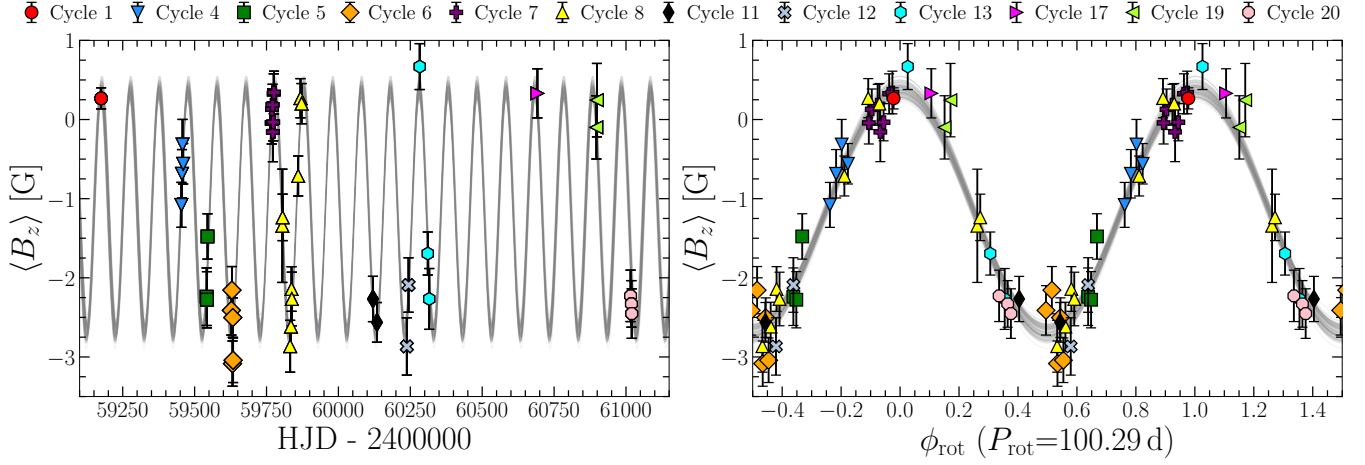


Figure 4. Polaris $\langle B_z \rangle$ measurements plotted as a function of HJD (left) and ϕ_{rot} (right). The marker shapes and colours denote N_{rot} . The grey lines show 100 random samples drawn from the MCMC joint posterior distribution.

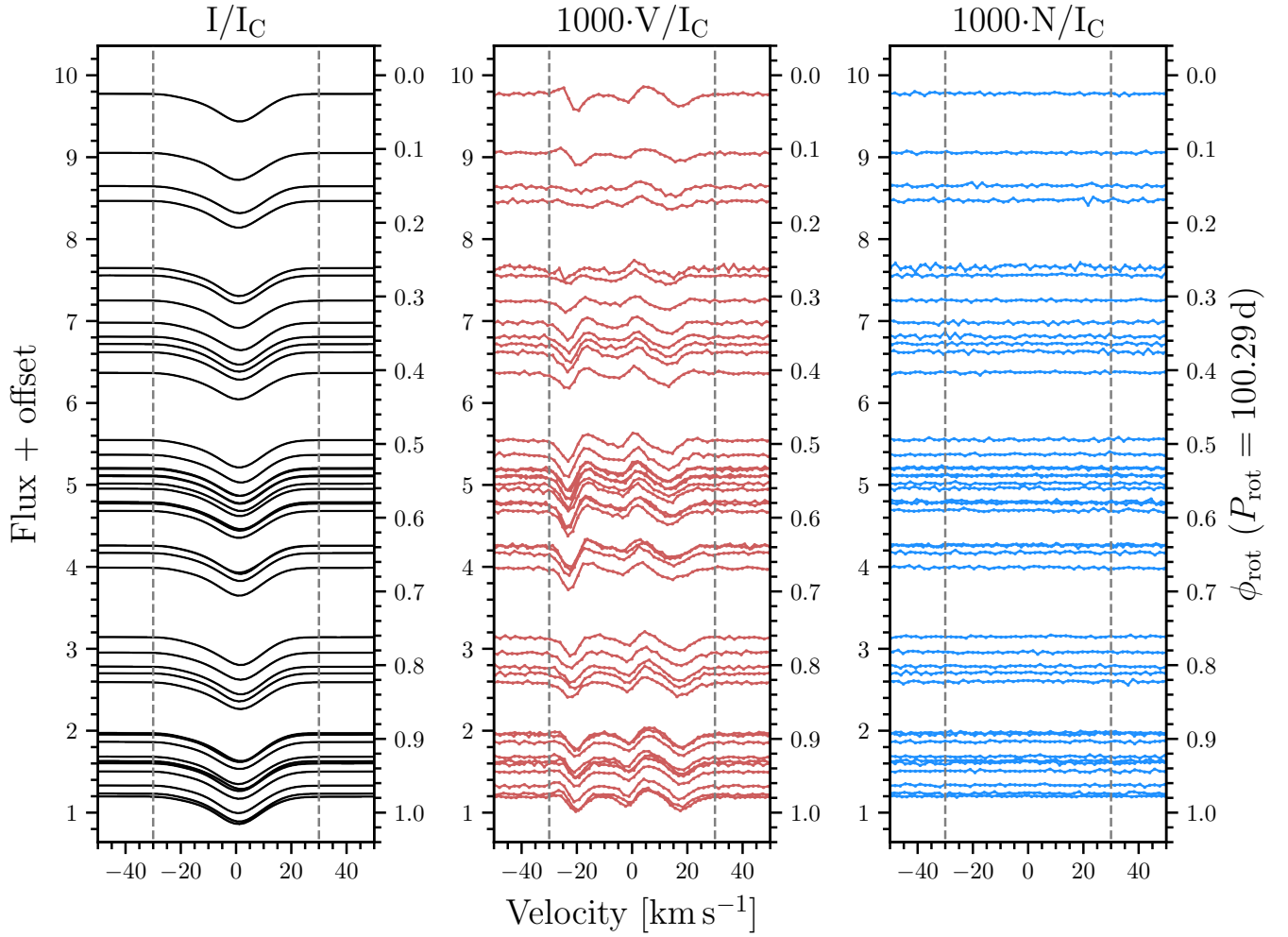


Figure 5. Continuum normalized and RV_{cog} corrected LSD profiles of Polaris plotted as a function of ϕ_{rot} . From left to right, LSD Stokes I (black), LSD Stokes V (red) and LSD N (blue). The vertical dashed gray lines mark the integration bounds in the FAP and $\langle B_z \rangle$ analysis.

5.3. Alias and Literature Periods

Figure 3 (second row) includes the residual $\langle B_z \rangle$ GLS periodogram after subtraction of the best fit model. No significant periods are detected in the residuals, suggesting that ~ 84.8 days and ~ 49.1 days are aliases of P_{rot} . We confirmed this by computing the GLS periodogram of the $\langle B_z \rangle$ model fit with the same time sampling and uncertainties as the observations. The model $\langle B_z \rangle$ power spectrum (Fig. 3, third row) is nearly identical to the power spectrum of the $\langle B_z \rangle$ measurements. Long period aliases are detected at ~ 84.8 days, ~ 49.1 days, ~ 43.3 days and ~ 25.7 days (FAP < 0.01).

For a stable magnetic field geometry, LSD Stokes V profiles obtained over multiple rotational cycles will show similar morphologies at similar rotation phases. As an additional check, we visually verified that the alias periods yield LSD Stokes V profiles with inconsistent morphologies at similar phases.

The 100.3 days signal is inconsistent with previously reported spectroscopic periodicities, including $\sim 60/120$ days which have been suggested as possible rotation periods (B.-C. Lee et al. 2008; R. I. Anderson 2019; K. Barbey et al. 2025). We phased the $\langle B_z \rangle$ measurements to the six long periods identified by K. Barbey et al. (2025), as well as ~ 40.2 days (A. P. Hatzes & W. D. Cochran 2000; R. I. Anderson 2019). None of these literature periods produced coherent $\langle B_z \rangle$ curves.

These results strengthen our interpretation of ~ 100.3 days as the stellar rotation period. We do not observe any other significant periodicity in the $\langle B_z \rangle$ data that is not an alias. The $\langle B_z \rangle$ variation is incompatible with previously published periods, including P_{puls} , and the variation has remained stable over ~ 5 years of observations.

5.4. Magnetic Field Strength and Pulsation

We do not observe significant changes in the LSD Stokes V profiles due to pulsation. Figure 6 shows Stokes I and V profiles obtained over three consecutive nights. The profiles span the ascending branch of the RV curve as the atmosphere expands from average radius to maximum radius and then contracts. No strong variability is observed in the LSD profiles. This is consistent with the absence of significant power near $P_{\text{puls}} \approx 3.97$ days in the $\langle B_z \rangle$ GLS periodogram (Fig 3).

The insensitivity of the Stokes V profiles to pulsation phase is not entirely unexpected given Polaris' low-amplitude pulsation. Under an assumption of magnetic flux conservation, a $\langle B_z \rangle$ modulation would not be detectable at the current amplitude. The surface magnetic

field strength is related to the radius by

$$\frac{B_{R_{\text{max}}}}{B_{R_{\text{min}}}} = \left(\frac{R_{\text{min}}}{R_{\text{max}}} \right)^2 \quad (8)$$

where $B_{R_{\text{max}}}$ and $B_{R_{\text{min}}}$ are the surface magnetic field strengths at maximum radius R_{max} and minimum radius R_{min} respectively. From the radius variation calculated in Sec. 5.1 we have $R_{\text{min}} \approx 46.1 R_{\odot}$ and $R_{\text{max}} \approx 46.5 R_{\odot}$. We define the cycle averaged surface field strength be $\langle B_{\text{puls}} \rangle = \frac{1}{2}(B_{R_{\text{max}}} + B_{R_{\text{min}}})$. For $\langle B_{\text{puls}} \rangle < 10$ G, Eq. 8 gives a total variation of < 0.2 G. This variation is too low to be detectable as it is below the precision of the $\langle B_z \rangle$ measurements.

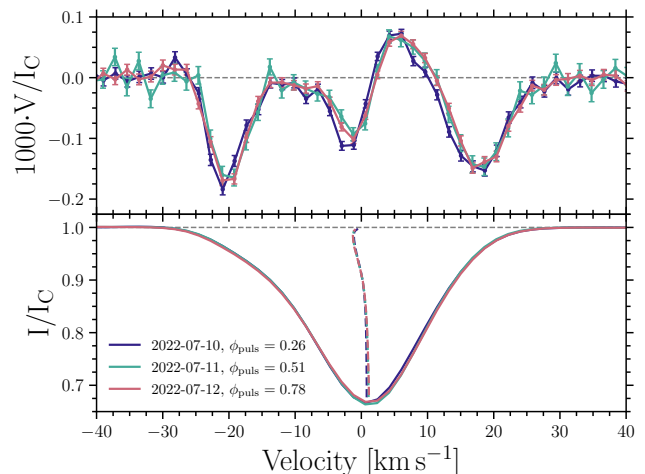


Figure 6. Continuum normalized and RV_{cog} corrected LSD Stokes V (top) and I (bottom) profiles over three consecutive nights. The Stokes I bisectors are shown by the vertical dashed lines. The observations sample the radial expansion from minimum to maximum radius (see Fig. 2). No strong variability is observed.

5.5. LSD Stokes I Bisectors

We calculated the bisector (D. F. Gray 1982) and associated bisector inverse span (BIS; D. Queloz et al. 2001) for each RV_{cog} -corrected LSD Stokes I profile. The calculations were performed using the `calc_bis` routine implemented in `SpecpolFlow`. The BIS is defined to be $\text{BIS} = \bar{v}_t - \bar{v}_b$ where \bar{v}_t , \bar{v}_b are the average velocities calculated respectively from the top 10–40% and bottom 60–90% of the Stokes I profile. Figure A1 shows the bisector variability across all observations.

We performed a period analysis on the BIS measurements similar to the $\langle B_z \rangle$ GLS analysis described in Sec. 5.2. Figure 7 shows the BIS GLS periodogram. No significant periods are detected at the FAP = 0.01 level. While not formally detected, peaks corresponding to P_{puls} and P_{rot} can be clearly identified. The

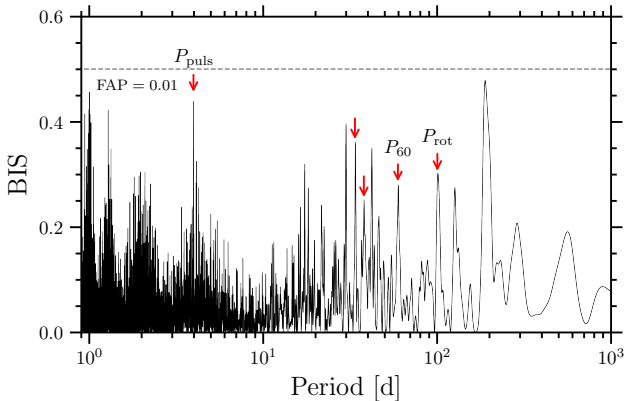


Figure 7. GLS periodogram of the BIS measurements. The horizontal dashed line denotes $FAP = 0.01$. No significant periods are detected. Peaks that correspond to P_{puls} , P_{rot} and $P_{60} \approx 60$ days are labelled and marked with red arrows. The unlabelled arrows mark ~ 33.7 days and ~ 37.9 days.

peak at ~ 59.5 days appears consistent with reports of a $P_{60} \approx 60$ day period (R. I. Anderson 2019; K. Barbey et al. 2025) and half the 119.1 days RV period reported by B.-C. Lee et al. (2008). Additionally, peaks at ~ 33.7 days and ~ 37.9 days are close to candidate signals reported by K. Barbey et al. (2025).

6. ROTATION, LINE BROADENING AND STELLAR INCLINATION

With a direct measurement of P_{rot} , the equatorial rotation velocity at mean radius is given by

$$v_{\text{eq}} = \frac{2\pi \langle R_{\star} \rangle}{P_{\text{rot}}}. \quad (9)$$

For $\langle R_{\star} \rangle = 46.27 \pm 0.42 R_{\odot}$ (N. R. Evans et al. 2024) and $P_{\text{rot}} = 100.29 \pm 0.19$ days we obtain a precise measurement of $v_{\text{eq}} = 23.3 \pm 0.2 \text{ km s}^{-1}$.

In principle the stellar inclination angle i_{\star} is determinable from a spectroscopic measurement of the projected equatorial rotation velocity $v_{\text{eq}} \sin i_{\star}$. The challenges in disentangling broadening mechanisms in slowly rotating, radial pulsators has been previously explored for Cepheids (D. Bersier & G. Burki 1996; D. Gillet et al. 1999; D. F. Gray & K. B. Stevenson 2007) and RR Lyraes (R. C. Peterson et al. 1996; G. W. Preston et al. 2019). Line asymmetries due to pulsation, velocity gradients and granulation complicate the separation of macroturbulent broadening v_{mac} and low $v_{\text{eq}} \sin i_{\star}$. We performed a spectral broadening analysis to investigate the correlation between $v_{\text{eq}} \sin i_{\star}$ and v_{mac} and the subsequent impact on our ability to constrain i_{\star} .

The broadening analysis was performed on the co-added RV_{cog}-corrected 2022-07-10 spectrum which was obtained at a ϕ_{puls} near mean radius (Fig. 2).

We first applied the line-depth ratio (LDR) method (V. V. Kovtyukh & N. I. Gorlova 2000) to measure $T_{\text{eff}} = 6030 \pm 10 \text{ K}$. We excluded LDRs that utilized the Ni II $\lambda 5755$ and Cr I $\lambda 6330$ lines due to telluric contamination. Our T_{eff} value is consistent with previous LDR measurements (I. A. Usenko et al. 2005; D. G. Turner et al. 2013; V. Ripepi et al. 2021). The stellar mass and radius (N. R. Evans et al. 2024) imply a surface gravity of $\log g = 1.82 \pm 0.03$.

Model Stokes I spectra were synthesized using the ZEEMAN spectrum synthesis code (J. D. Landstreet 1988; G. A. Wade et al. 2001). We adopted a grid of plane-parallel ATLAS9 atmosphere models (R. L. Kurucz 1970; R. Kurucz 1993; F. Castelli & R. L. Kurucz 2003) assuming local thermodynamic equilibrium. The rotational broadening in ZEEMAN is implemented by applying local Doppler shifts to the sub-divided stellar disc. The code utilizes a radial-tangential model for v_{mac} (D. F. Gray 1975; D. F. Gray 2022). The spectral fitting was performed using a Levenberg-Marquardt χ^2 minimization procedure (W. H. Press et al. 1992) described by C. P. Folsom et al. (2012).

We first performed a simultaneous fitting of three spectral regions: 5500 – 5673 Å, 6050 – 6176 Å and 6365 – 6432 Å. These regions were chosen to minimize the impacts of severe line blending and telluric contamination. To help break degeneracies between parameters we fixed $T_{\text{eff}} = 6030 \text{ K}$ and $\log g = 1.82$. We allowed individual elemental abundances and the RV to vary. The best fit values for the broadening parameters were $v_{\text{eq}} \sin i_{\star} = 1.3 \pm 1.4 \text{ km s}^{-1}$, $v_{\text{mac}} = 14.8 \pm 0.2 \text{ km s}^{-1}$ and microturbulence $v_{\text{mic}} = 4.14 \pm 0.02 \text{ km s}^{-1}$.

We then selected five metal lines to perform a detailed broadening analysis: Fe I $\lambda 5576$, Fe I $\lambda 6066$, Fe I $\lambda 6125$, Si I $\lambda 6421$ and Fe I $\lambda 6431$. The chosen lines are well reproduced by the best fit model, do not have significant blends or telluric contamination and have depths less than 50% of the continuum. The line profiles and associated bisectors are shown in the left column of Fig A2. Similar to the LSD Stokes I profiles, the selected lines all show some degree of asymmetry in the blue wing. To verify that our results were not sensitive to the asymmetries, we symmetrized the line profiles by interpolating the red wing onto the wavelength grid of the blue wing. The symmetrized lines are shown in the right column of Fig A2.

To explore the correlation between $v_{\text{eq}} \sin i_{\star}$ and v_{mac} we generated χ^2 contour plots for the observed and symmetrized line profiles. For the χ^2 calculations the v_{mic} and the elemental abundances were fixed to the values obtained from fitting the large spectral regions. The RV was again allowed to vary. Figure 8 shows the

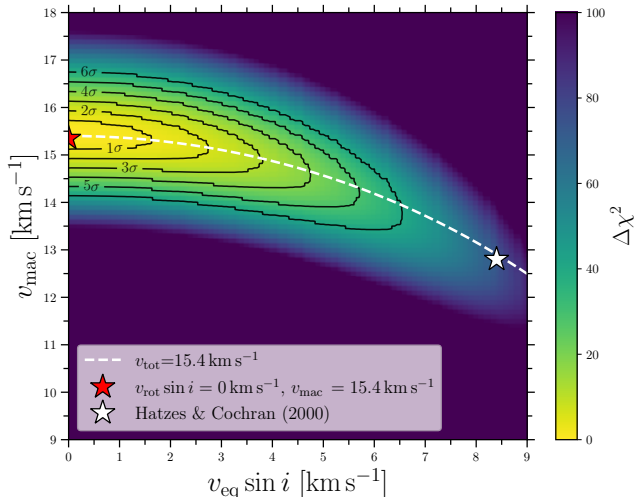


Figure 8. $\Delta\chi^2$ as a function of $v_{\text{eq}} \sin i_*$ and v_{mac} from fits to the five observed metal line profiles.

$\Delta\chi^2 = (\chi^2 - \chi_{\text{min}}^2) / \chi_{\nu, \text{min}}^2$ surface for fits to the five observed line profiles. We normalized by $\chi_{\nu, \text{min}}^2$ to help account for systematic differences between the model and observations. A similar $\Delta\chi^2$ plot for the symmetrized profiles is shown in Fig A3. The best fit models to the five observed and five symmetrized line profiles minimize rotational broadening ($v_{\text{eq}} \sin i_* \approx 0 \text{ km s}^{-1}$), giving $v_{\text{mac}} \approx 15 \text{ km s}^{-1}$. However, a strong correlation between $v_{\text{eq}} \sin i_*$ and v_{mac} is observed in the $\Delta\chi^2$ plots, which roughly traces the total combined broadening $v_{\text{tot}} = \sqrt{(v_{\text{eq}} \sin i_*)^2 + (v_{\text{mac}})^2}$.

To the best of our knowledge A. P. Hatzes & W. D. Cochran (2000) provide the most recent literature measurement of Polaris’ $v_{\text{eq}} \sin i_*$. The authors report $v_{\text{eq}} \sin i_* = 8.4 \text{ km s}^{-1}$ and a macroturbulent velocity of $v_{\text{mac}} = 12.8 \text{ km s}^{-1}$ from a fit to the Sc II $\lambda 5526$ line from spectra with $R \sim 50,000$. Our fitting of both the spectral regions and selected line profiles suggests low to absent rotational broadening, inconsistent with the findings of A. P. Hatzes & W. D. Cochran (2000). However, as shown in Fig 8 the broadening values given by A. P. Hatzes & W. D. Cochran (2000) lie close to the same $v_{\text{tot}} = 15.4 \text{ km s}^{-1}$ curve as our best fit values. This suggests that the discrepancy between our results is due to modelling systematics from the assumption of the form for v_{mac} .

From our analysis we conclude that we cannot confidently disentangle the broadening parameters from χ^2 fitting. To set upper limits on $v_{\text{eq}} \sin i_*$ we fixed $v_{\text{mac}} = 0 \text{ km s}^{-1}$ and fit the five observed and symmetrized line profiles obtaining $v_{\text{eq}} \sin i_* = 13.5 \pm 0.1 \text{ km s}^{-1}$ and $v_{\text{eq}} \sin i_* = 13.3 \pm 0.1 \text{ km s}^{-1}$ respectively. The model

fits are shown in Fig. A2. From these results we set a conservative upper bound of $v_{\text{eq}} \sin i_* < 13.5 \text{ km s}^{-1}$.

From $v_{\text{eq}} = 23.3 \pm 0.2 \text{ km s}^{-1}$ and $v_{\text{eq}} \sin i_* < 13.5 \text{ km s}^{-1}$ we set a conservative upper bound of $i_* < 37^\circ$ on the stellar inclination angle (for $0^\circ \leq i_* \leq 90^\circ$). Assuming $v_{\text{eq}} \sin i_* = 8.4 \text{ km s}^{-1}$ from A. P. Hatzes & W. D. Cochran (2000) would imply a lower inclination of $\sim 21^\circ$.

7. BINARY SPIN-ORBIT MISALIGNMENT

We investigated our ability to set constraints on the spin orbit alignment of Polaris Aa. We work in the standard coordinate system where \hat{x} and \hat{y} are in the tangent plane of the sky and \hat{z} points along the line of sight away from the observer. The unit normal vector to the orbital plane is given by

$$\hat{n}_o = \begin{bmatrix} \sin(i_o) \sin(\Omega_o) \\ -\sin(i_o) \cos(\Omega_o) \\ \cos(i_o) \end{bmatrix} \quad (10)$$

where i_o is the orbital inclination angle and Ω_o is the longitude of the ascending node (R. W. Hilditch 2001). The obliquity angle β between \hat{n}_o and the stellar rotation axis \hat{n}_* is then given by

$$\beta = \cos^{-1}(\hat{n}_o \cdot \hat{n}_*). \quad (11)$$

We calculated the probability density function (PDF) of β through Monte Carlo sampling. To sample \hat{n}_o we adopted Gaussian priors for i_o and Ω_o using the most likely values and 1σ uncertainties from the “replicated” weighted solution reported by N. R. Evans et al. (2024). We sampled $\hat{n}_* = (\sin \theta \cos \phi \ \sin \theta \sin \phi \ \cos \theta)$ in spherical coordinates where θ is the polar angle and ϕ is the azimuthal angle. From our analysis in Sec. 6 we have the constraint $i_* < 37^\circ$. Circular polarization alone cannot resolve the 180° ambiguity on i_* . As $i_o \approx 128^\circ$, \hat{n}_o points towards the observer (Eq. 10). Therefore \hat{n}_* is prograde with respect to the orbit when $\theta \in [143^\circ, 180^\circ]$. We consider only the prograde solution in our analysis as it is the most likely. A rotation axis retrograde to the orbit would clearly indicate an extreme dynamical interaction in Polaris’ past.

We sampled $\cos \theta$ uniformly for θ over the range $[143^\circ, 180^\circ]$. For ϕ we sampled uniformly over the range $[0^\circ, 360^\circ]$. We generated 10^6 samples of β using Eq. 11 to estimate the PDF shown in Figure 9. The PDF shows a high likelihood of a strong misalignment between \hat{n}_* and \hat{n}_o with median $\beta \approx 55.4^\circ$ and a 95% confidence interval (CI) of $[21.4^\circ, 85.4^\circ]$. The PDF gives a lower bound of $\beta > 18.7^\circ$ at 99% confidence.

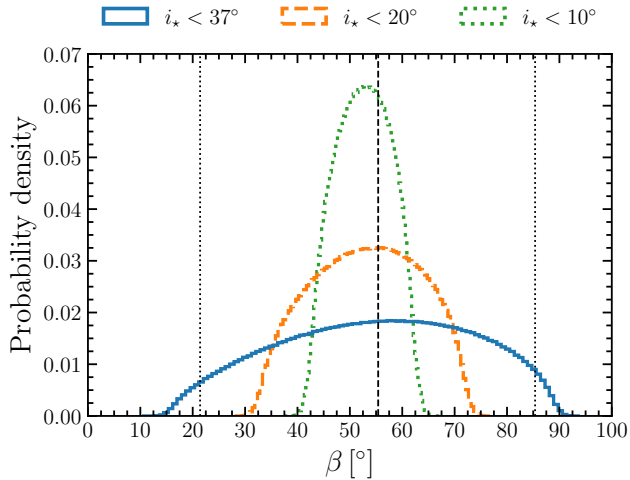


Figure 9. Probability density functions for the obliquity angle β between the stellar rotation axis \hat{n}_* and orbital normal axis \hat{n}_o assuming the stellar rotation is prograde relative to the orbit. The solid blue line denotes the distribution for $i_* < 37^\circ$. The vertical dashed line denotes the median $\beta \approx 55.4^\circ$ value of the distribution, and the vertical dotted lines denote the 95% CI. The dashed orange and dotted green lines show PDFs assuming improved constraints on i_* .

Our constraint on i_* is a conservative upper bound and may be improved in future work through magnetic mapping or interferometric imaging. In Figure 9 we also show PDFs assuming improved constraints of $i_* < 20^\circ$ and $i_* < 10^\circ$.

8. DISCUSSION

8.1. Rotational Properties

We have performed the first direct measurement of P_{rot} and v_{eq} for a Cepheid, demonstrating the power of magnetometry for determining the rotation properties of evolved, intermediate-mass and massive stars. Our measurement of P_{rot} is inconsistent with previously reported spectroscopic periods (e.g. K. Barbey et al. 2025). This indicates that these signals have physical origins likely unrelated to rotation. While we do not detect any formally significant periods in the BIS measurements, a peak at P_{rot} is distinguishable in the GLS periodogram (Fig. 7). This suggests that the signal at P_{rot} may be present in long spectroscopic time series, but is weaker than other sources of variability.

While detailed evolutionary modelling that incorporates rotational constraints is outside the scope of this work, we compare our results to fiducial Geneva models (S. Ekström et al. 2012; C. Georgy et al. 2013) with which R. I. Anderson et al. (2016) performed a pulsational instability analysis. R. I. Anderson et al. (2016) report v_{eq} at IS boundaries for non-rotating ($\omega = 0$),

moderately rotating ($\omega = 0.5$) and fast-rotating ($\omega = 0.9$) models where $\omega = \Omega/\Omega_{\text{crit}}$ and Ω_{crit} is the critical angular velocity. The properties of Polaris most closely match a first-overtone, $5 M_\odot$, $Z = 0.014$ model at the blue edge of the IS (R. I. Anderson et al. 2016, Table A.4.). The crossing number of Polaris has been debated between 1st and 3rd (see Sec. 8.2). For $\omega = 0.5$ the authors report $v_{\text{eq}} = 28 \text{ km s}^{-1}$ for the 1st crossing and $v_{\text{eq}} = 16.9 \text{ km s}^{-1}$ for the 3rd crossing. For $\omega = 0.9$ the authors report $v_{\text{eq}} = 55.6 \text{ km s}^{-1}$ for the 1st crossing and $v_{\text{eq}} = 17.8 \text{ km s}^{-1}$ for the 3rd crossing.

Our measurement of $v_{\text{eq}} \approx 23 \text{ km s}^{-1}$ confidently rules out a 1st crossing with fast rotation ($\omega = 0.9$). This is consistent with model predictions for the CNO abundances (R. I. Anderson 2018). The absolute discrepancy between the measured v_{eq} and that predicted by 1st and 3rd crossings with $\omega = 0.5$ and a 3rd crossing with $\omega = 0.9$ is similar. Therefore, we cannot clearly distinguish between these scenarios from v_{eq} alone.

8.2. Uncertain Origin of the Magnetic Field

The magnetic properties of Polaris are challenging to reconcile with our current understanding of magnetism in intermediate-mass stars. The variability in Polaris' LSD Stokes V profiles and $\langle B_z \rangle$ measurements has remained remarkably stable over five years of observations, spanning ~ 18 rotation cycles and ~ 460 pulsation cycles. The stability of Polaris' magnetic field is reminiscent of the so-called 'fossil fields' observed in a subset ($< 10\%$) of hot, main-sequence (MS) stars with spectral types O, B and A (T. Morel et al. 2015; L. Fossati et al. 2015; G. A. Wade et al. 2016; J. Sikora et al. 2019a; V. Petit et al. 2019). Fossil magnetic fields tend to be strong (order 100 G to 10 kG), with predominantly dipolar geometries that are stable over decades (M. E. Oksala et al. 2012; J. Silvester et al. 2014; J. H. Grunhut et al. 2017; M. E. Shultz et al. 2018; J. Sikora et al. 2019b).

However, Polaris' Stokes V profiles do not resemble those of a simple dipole. The Stokes V profiles are complex with multiple polarity reversals across the $V/I_C = 0$ axis. This morphology is qualitatively similar to the Stokes V signatures observed in low-mass MS stars, which commonly possess complex magnetic field geometries and convective dynamo driven variability cycles (C. P. Folsom et al. 2016, 2018; J.-F. Donati et al. 2023; S. Bellotti et al. 2025).

The apparent tension between the stability and complexity of Polaris' magnetic signature highlights our incomplete understanding of magnetism in evolved intermediate and massive stars. Specifically, the complex relationship between magnetic fields, convection, pulsa-

tion and changes in internal structure as stars transition across instability regions.

As a $\sim 5 M_{\odot}$ F8Ib yellow-supergiant, Polaris' progenitor was presumably a mid B-type star on the MS, comprised of a convective core with a primarily radiative outer envelope and near surface He II convection zone (M. Cantiello & J. Braithwaite 2019; A. S. Jermyn et al. 2022). As the star cooled and expanded, shallow H and He I convection zones formed, helping to drive the stellar pulsation in the IS (G. Bono et al. 1999; M. Stuck et al. 2025). C. Charbonnel et al. (2017) do not predict an $\alpha - \omega$ dynamo at this evolutionary stage due to the inefficiency of the thin, outer convective envelope. After crossing the IS, an intermediate-mass star will develop a deep convective envelope on the red giant branch. Weak surface magnetic fields have been directly detected in red giants (M. Aurière et al. 2009, 2015; A. Borisova et al. 2016; S. Tsvetkova et al. 2017), and are believed to be generated by convective dynamos (C. Charbonnel et al. 2017; L. Amard et al. 2024).

After ignition of core helium burning, a $5 M_{\odot}$ star will move back through the IS on a blue loop for second and third crossings, and the outer envelope will transition back from convective to primarily radiative. The impact of this transition on an envelope magnetic field is unclear. Persistence of magnetic fields between convective and radiative regimes is observed in other stellar contexts. Magnetic fields are detected in intermediate mass Herbig Ae/Be and T Tauri stars with a similar incidence rate to their MS counterparts (G. A. Wade et al. 2007; E. Alecian et al. 2013; F. Villebrun et al. 2019). This suggests that magnetic fields generated during convective pre-main sequence stages may relax into stable fossil-field configurations on the MS (C. Neiner et al. 2015). Strong magnetic fields ($> 10^5$ G) detected in the radiative cores of red giants through asteroseismic techniques are believed to be fossil-field remnants from dynamos that operated during the convective core stage on the MS (J. Fuller et al. 2015; L. Bugnet et al. 2021). There is also a small subset of red giants that are hypothesized to be the descendants of strongly magnetic Ap-type stars due to anomalously high activity levels and $\langle B_z \rangle$ strengths for their rotation rate (K. Stepien 1993; M. Aurière et al. 2015; A. Borisova et al. 2016).

It is challenging to ascribe a firm origin for the magnetic field due to the ambiguity surrounding Polaris' crossing number. The predominantly positive rate of period change \dot{P} over the last ~ 175 years (G. Torres 2023) suggests an increasing R_* and a 1st or 3rd crossing. Authors have argued a 1st (D. G. Turner et al. 2013; Y. A. Fadeyev 2015; R. I. Anderson 2018; V. Ripepi et al. 2021) or 3rd (H. R. Neilson 2014; N. R. Evans

et al. 2018) crossing based on the luminosity, \dot{P} and CNO abundances. Conflicting interpretations are partially due to the historical disagreement over the distance to Polaris A (S. G. Engle et al. 2018). If Polaris is on its 1st crossing than the magnetic field may be of fossil origin, or there is a dynamo mechanism efficient enough to generate and sustain the global field. Such a dynamo would be presumably generated in the sub-surface convective zones. If Polaris is on its 3rd crossing, then we should consider the possibility that a magnetic field generated during the red-giant phase can persist as a type of fossil field through blue loops.

8.3. Comparison with the Broader Cepheid Sample

Polaris' magnetic signature is also challenging to interpret in the context of our larger magnetic survey of Cepheids. In addition to Polaris, J. A. Barron et al. (2022) reported magnetic detections in δ Cep, η Aql and ζ Gem. In contrast to Polaris, these targets show strongly asymmetric single- or double-lobed Stokes V profiles. We observe similar features in most other detected survey targets, which are the subject of a forthcoming paper (J. A. Barron et al. 2024, in prep.). A notable exception is the complex Stokes V signature of MY Pup (J. A. Barron et al. 2024). Like Polaris, MY Pup ($P_{\text{puls}} = 5.7$ d; F7Ib/II) is a first overtone pulsator (F. Kienzle et al. 1999; V. Hocdé et al. 2024) with a pulsation amplitude larger than Polaris, but low relative to fundamental Cepheids with similar P_{puls} .

Stokes V asymmetries and shock enhancement have been observed in other evolved pulsators, including the Mira χ Cyg (A. Lèbre et al. 2014; A. Lavail et al. 2025) and the RV Tauri stars R Sct and U Mon (L. Sabin et al. 2015; S. Georgiev et al. 2023). Notably, net positive circular polarization has also been detected in the rotationally averaged Stokes V profiles of three weakly magnetic Am stars (P. Petit et al. 2011; A. Blazère et al. 2016). As A. Blazère et al. (2016) discuss, similarly anomalous Stokes V signatures are detected in solar magnetic regions and arise from velocity and magnetic field gradients along the line of sight (A. López Ariste 2002; M. J. Martínez González et al. 2008; L. Bellot Rubio & D. Orozco Suárez 2019). In the case of Am stars A. Blazère et al. (2016) suggest that the thin convective layer near the surface may generate the necessary velocity and magnetic field gradients (F. Kupka et al. 2009). C. P. Folsom (2018) demonstrated that inclusion of atmospheric gradients in polarized spectrum synthesis models can qualitatively reproduce Am star single lobed Stokes V signatures. Such a modelling approach has not yet been applied to Cepheids.

8.4. Comparison with Non-Cepheid Supergiants

Magnetic detections are rare among massive ($\gtrsim 8 M_{\odot}$) post-MS B and A-type supergiants (E. Verdugo et al. 2003; C. Aerts et al. 2013; M. Shultz et al. 2014). The handful of magnetically detected A-type supergiants possess weak (~ 1 G) $\langle B_z \rangle$ strengths and Stokes V signatures consistent with a dipole field, suggesting they may be the evolved descendants of fossil field hosting MS OB-type stars (C. Neiner et al. 2017; A. J. Martin et al. 2018; G. A. Wade et al. 2025). At cooler temperatures, magnetic fields have been detected in a small number of non-Cepheid F, G and K-type supergiants (J. H. Grunhut et al. 2010). Similar to the A supergiants, these stars have weak $\langle B_z \rangle$ strengths but present a wider variety of Stokes V morphologies. G. A. Wade et al. (2025) recently presented magnetic monitoring of the F-type supergiants α Lep (F0Ib) and α Per (F5Ib). The authors suggested a dynamo origin for the fields due to the complexity and variability of the Stokes V signatures.

The Stokes V signatures of α Per bear strong resemblance to those of Polaris, both in their complexity and asymmetry about $V/I_C = 0$. Previously suggested to be a low-amplitude Cepheid, α Per lies outside the blue edge of the IS (A. P. Hatzes & W. D. Cochran 1995) and presents multiple long periods of uncertain origin (B.-C. Lee et al. 2012; T.-Y. Bang et al. 2025; G. A. Wade et al. 2025). In light of our results, we suggest an alternative explanation to G. A. Wade et al. (2025) for α Per's Stokes V variability. Like Polaris, α Per may host a complex but stable magnetic field configuration. In this scenario, the differences in Stokes V variability may be attributed to Polaris' low inclination angle relative to α Per (Sec. 6). More observations of α Per are needed to confidently determine a rotation period and test this hypothesis. Detections in additional targets are required to determine if the Stokes V morphology of α Per is typical of non-Cepheid mid to late F-type supergiants.

8.5. Merger Hypothesis

H. E. Bond et al. (2018) identified a large age discrepancy between the Cepheid Polaris Aa and the wide companion Polaris B (F6V) from isochrone modelling in the $B - V$ colour magnitude diagram. N. R. Evans et al. (2018) estimate an approximate age of 100 Myr for Polaris A and 2.25 Gyr for Polaris B. Assuming that Polaris B is a physically associated, coeval companion of Polaris Aa, this tension may be explained if Polaris Aa is a merger product (H. E. Bond et al. 2018; N. R. Evans et al. 2018).

A merger scenario is interesting to consider in the context of Polaris' magnetic field. Stellar mergers appear to be a viable channel to produce some of the strongly magnetic O and B-type stars on the MS (F. R. N. Schneider et al. 2016, 2019; P. Vynatheya et al. 2026). As we discuss in Sec. 8.2, Polaris' Stokes V signatures do not resemble the simple dipole signatures commonly associated with fossil-field hosting progenitors. However, we have little observational evidence concerning the long-term stability of magnetic fields produced through binary interaction, and how fossil-fields respond to the development of envelope convection as the star evolves.

In Sec. 8.1 we used results from standard evolutionary tracks to show that v_{eq} is inconsistent with Polaris being a first-crossing Cepheid with near critical rotation on the MS. As F. R. N. Schneider (2025) discuss the immediate products of most stellar mergers can be assumed to be rotating near the break-up velocity. However, merged stars may spin down efficiently, losing angular momentum through their remnant disc and magnetic braking to become slow rotators. There is some observational evidence to support this, as F. R. Ferraro et al. (2023) found that slower rotating blue stragglers prefer higher density environments with high collision rates. Merger products may also possess different interior structures than their single star counterparts, complicating evolution modelling (E. P. Bellinger et al. 2024; J. Henneco et al. 2024).

The spin-orbit misalignment of Polaris Aa may also be consistent with a past dynamical interaction. Further investigation of Polaris as a potential merger product should include detailed evolutionary modelling and N body simulation.

8.6. Future Work

Future work should explore reconstruction of the large-scale magnetic field geometry through inversion methods such as Zeeman Doppler Imaging (ZDI; O. Kochukhov 2016). A magnetic mapping may aid in further constraining the stellar inclination angle and in turn the degree of spin-orbit misalignment. Additionally, a magnetic map could be compared to interferometric surface reconstructions (N. R. Evans et al. 2024) to search for correlations between the distribution of surface spots and the magnetic field geometry. However, reconstructing the surface field presents several challenges. Additional spectropolarimetric observations are needed over some rotational phases, particularly between $\phi_{\text{rot}} = 0$ and $\phi_{\text{rot}} = 0.3$ (Fig. 5). To perform a magnetic inversion, the stellar pulsation and asymmetry of the LSD Stokes V profiles will likely need to be considered.

Long-term magnetic monitoring of Polaris is necessary to examine the field’s stability and obtain further insight into the field’s origins. Continued observation will also probe the possible relation between magnetic field strength and changing pulsation amplitude due to magnetoconvective cycles (R. B. Stothers 2009).

A key challenge in our study of Polaris has been constraints on the frequency and duration of ESPaDOnS mountings due to competitive pressure from other CFHT instruments. These limitations will be partially alleviated with the upcoming installation of the Wenaokeao optomechanical interface. Wenaokeao will provide simultaneous mounting of ESPaDOnS and the SPIRou near-infrared spectropolarimeter, increasing the number of nights ESPaDOnS is mounted per semester. We expect that this will aid in the continued study of Polaris and other slowly rotating stars including blue, yellow and red supergiants.

9. CONCLUSIONS

We analyzed 42 optical spectropolarimetric observations of Polaris obtained with ESPaDOnS between 2020 and 2025. Here we list the key conclusions of our study.

1. A complex LSD Stokes V magnetic signature is detected in all spectropolarimetric observations. The Stokes V profiles are not strongly variable over single pulsation cycles, but are variable over long time spans.
2. The $\langle B_z \rangle$ measurements vary between -3 G and $+0.6$ G. The $\langle B_z \rangle$ measurements are obtained at high precision with typical uncertainties of ~ 0.3 G.
3. From a period analysis of the $\langle B_z \rangle$ measurements we infer a rotation period of $P_{\text{rot}} = 100.29 \pm 0.19$ days. No other significant periods are detected in the $\langle B_z \rangle$ measurements. The $\langle B_z \rangle$ measurements vary sinusoidally when phased to P_{rot} , and the variability is stable over the 5 year observing span.
4. From P_{rot} and previous determination of $\langle R_\star \rangle$ we obtain a precise measurement of the equatorial rotation velocity $v_{\text{eq}} = 23.3 \pm 0.2 \text{ km s}^{-1}$.
5. We are unable to confidently disentangle spectral line broadening contributions from $v_{\text{eq}} \sin i_\star$ and v_{mac} . We set a conservative upper limit of $v_{\text{eq}} \sin i_\star < 13.5 \text{ km s}^{-1}$. This constrains the stellar inclination to $i_\star < 37^\circ$.
6. We set a lower bound of $\beta > 18.7^\circ$ on the obliquity between the stellar rotation and orbital axes.

There is a high probability that the axes are strongly misaligned.

7. The origin of Polaris’ magnetic field remains unclear. The apparent tension between the complexity of the Stokes V signatures and long term stability of the $\langle B_z \rangle$ measurements makes it challenging to attribute Polaris’ magnetic field to a fossil-field or $\alpha - \omega$ dynamo model.
8. Future work should explore reconstruction of the surface magnetic field geometry. A magnetic map could be compared to interferometric surface reconstructions to look for correlations between the magnetic field geometry and surface features.

ACKNOWLEDGMENTS

We are grateful to Dr. Nadine Manset for assistance with scheduling the observations and questions regarding data reduction. We thank Dr. Richard Anderson for helpful discussions.

JAB acknowledges support through a Postgraduate Doctoral Scholarship (PGS D) from the Natural Sciences and Engineering Research Council (NSERC) of Canada. GAW acknowledges support in the form of a Discovery Grant from the Natural Sciences and Engineering Research Council (NSERC) of Canada. CPF acknowledges funding from the European Union’s Horizon Europe research and innovation programme under grant agreement No. 101079231 (EXOHOST), and from the United Kingdom Research and Innovation (UKRI) Horizon Europe Guarantee Scheme (grant number 10051045).

Based on observations obtained at the Canada-France-Hawai’i Telescope (CFHT) which is operated by the National Research Council of Canada, the Institut National des Sciences de l’Univers of the Centre National de la Recherche Scientifique of France, and the University of Hawai’i. CFHT is located on Maunakea on Hawai’i Island, a mountain of considerable cultural, natural, and ecological significance. Maunakea is a sacred site to Native Hawaiians, also known as Kānaka ‘Ōiwi. We would like to thank the Canada-France-Hawai’i Telescope (CFHT) Operations and Software Groups for their contributions and diligence in maintaining observatory operations; the CFHT Astronomy Group for their observation coordination and data acquisition efforts; and the CFHT Finance & Administration Group for their contributions to the management and administration of the observatory.

This research used the facilities of the Canadian Astronomy Data Centre operated by the National Research

Council of Canada with the support of the Canadian Space Agency. This work has made use of the VALD database, operated at Uppsala University, the Institute of Astronomy RAS in Moscow, and the University of Vienna. This research has made use of the SIMBAD database, operated at CDS, Strasbourg, France, and NASA’s Astrophysics Data System (ADS).

Software: astropy (Astropy Collaboration et al. 2022), corner (D. Foreman-Mackey 2016), emcee (D. Foreman-Mackey et al. 2013), Matplotlib (J. D. Hunter 2007), NumPy (C. R. Harris et al. 2020), SpecpolFlow (C. P. Folsom et al. 2025), ZEEMAN (J. D. Landstreet 1988; G. A. Wade et al. 2001)

Facilities: CFHT (ESPaDOnS)

APPENDIX

A. FIGURES AND TABLES

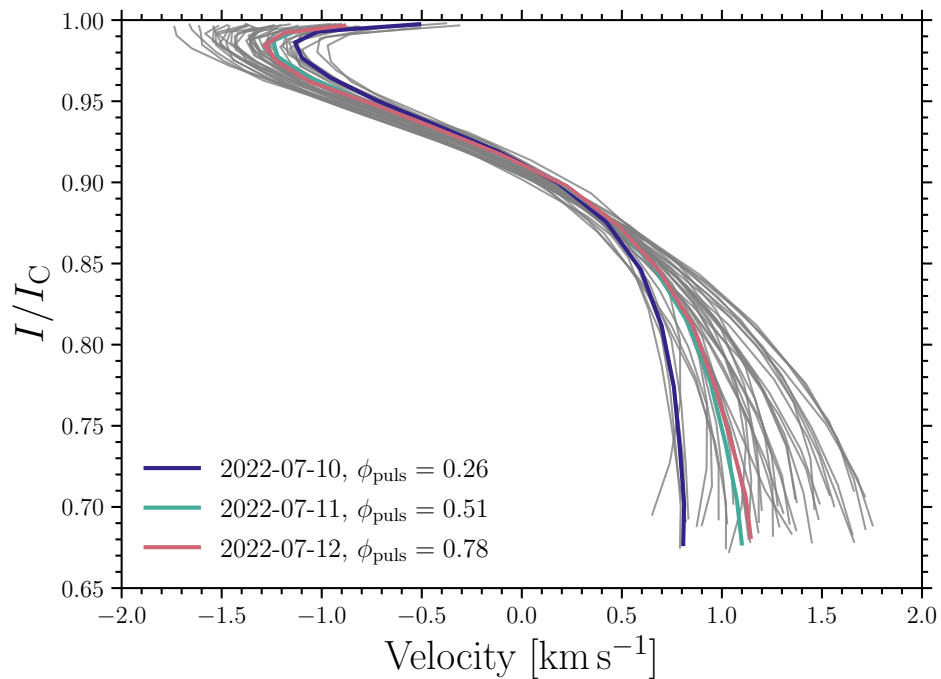


Figure A1. Bisector variability in the RV_{cog} corrected LSD Stokes I profiles. The coloured lines correspond to the LSD profiles shown in Fig. 6.

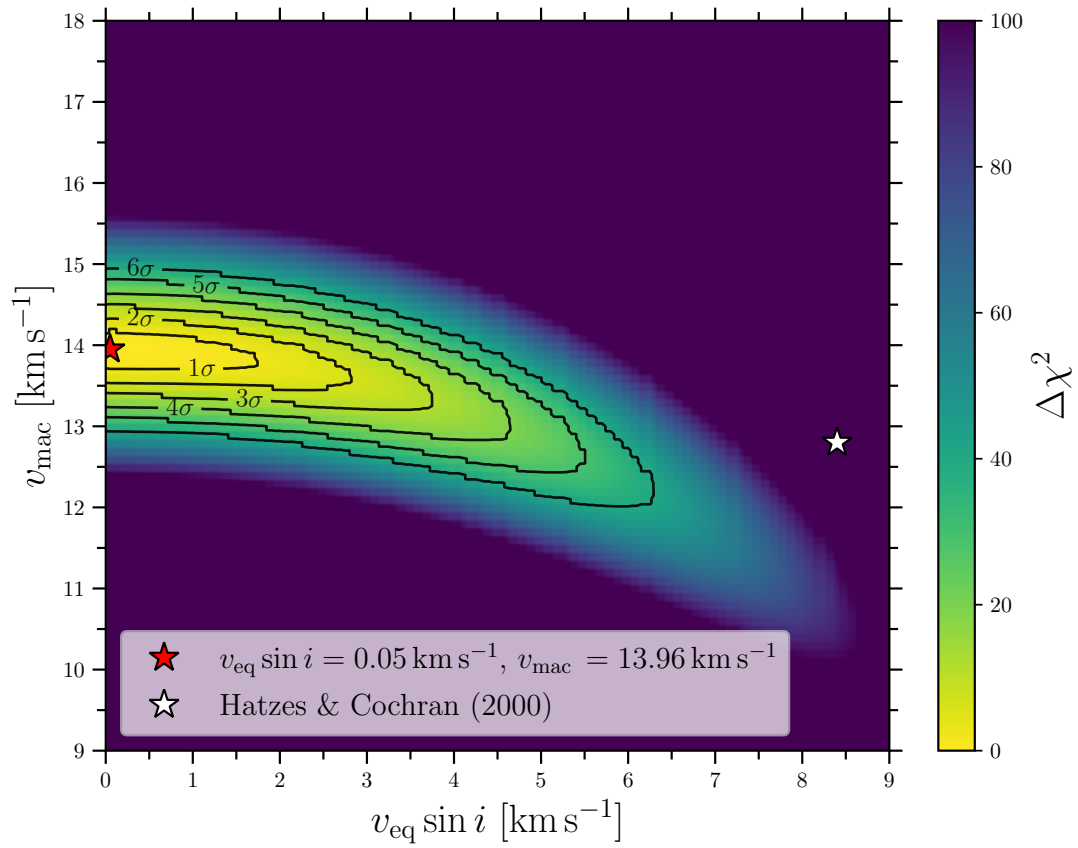


Figure A3. $\Delta\chi^2$ as a function of $v_{\text{eq}} \sin i_*$ and v_{mac} from fits to the five symmetrized metal line profiles.

Table A1. Log of ESPaDOnS spectropolarimetric observations of Polaris.

Date	HJD – 2 400 000	Exp. Time (s)	S/N (500 nm)	$\langle B_z \rangle$ (G)	RV_{cog} (km s ⁻¹)	RV_{corr} (km s ⁻¹)	ϕ_{puls}	ϕ_{rot}	N_{rot}
2020-11-21	59174.7863	56 × 4 × 11	6640	0.27 ± 0.13	-16.23 ± 0.04	-1.47 ± 0.06	0.143 ± 0.003	0.98 ± 0.02	1
2021-08-27	59453.9480	12 × 4 × 11	3190	-1.08 ± 0.28	-15.92 ± 0.04	-0.72 ± 0.06	0.426 ± 0.002	0.76 ± 0.01	4
2021-08-29	59456.0836	12 × 4 × 11	2780	-0.69 ± 0.31	-14.84 ± 0.03	0.37 ± 0.06	0.964 ± 0.002	0.78 ± 0.01	4
2021-08-31	59457.9845	11 × 4 × 11	2820	-0.32 ± 0.32	-15.73 ± 0.04	-0.52 ± 0.06	0.442 ± 0.002	0.80 ± 0.01	4
2021-09-02	59460.1018	12 × 4 × 11	3330	-0.56 ± 0.26	-14.99 ± 0.03	0.23 ± 0.06	0.975 ± 0.002	0.82 ± 0.01	4
2021-11-23	59541.8165	8 × 4 × 11	2360	-2.24 ± 0.36	-14.96 ± 0.04	0.38 ± 0.06	0.548 ± 0.002	0.64 ± 0.01	5
2021-11-24	59542.8842	11 × 4 × 11	2510	-2.28 ± 0.36	-13.88 ± 0.03	1.46 ± 0.06	0.817 ± 0.002	0.65 ± 0.01	5
2021-11-26	59544.8267	12 × 4 × 11	3050	-1.48 ± 0.29	-17.06 ± 0.04	-1.72 ± 0.06	0.306 ± 0.002	0.67 ± 0.01	5
2022-02-17	59627.7469	12 × 4 × 11	2790	-2.41 ± 0.31	-17.02 ± 0.04	-1.57 ± 0.05	0.182 ± 0.002	0.50 ± 0.01	6
2022-02-19	59629.7593	12 × 4 × 11	2890	-2.16 ± 0.30	-13.78 ± 0.03	1.67 ± 0.05	0.689 ± 0.002	0.52 ± 0.01	6
2022-02-21	59631.7122	12 × 4 × 11	3020	-3.08 ± 0.29	-16.96 ± 0.04	-1.51 ± 0.05	0.181 ± 0.002	0.53 ± 0.01	6
2022-02-22	59632.7124	12 × 4 × 11	3700	-2.50 ± 0.25	-16.11 ± 0.04	-0.65 ± 0.05	0.433 ± 0.002	0.54 ± 0.01	6
2022-02-23	59633.7124	12 × 4 × 11	3210	-3.04 ± 0.28	-13.87 ± 0.03	1.59 ± 0.05	0.684 ± 0.002	0.55 ± 0.01	6
2022-07-07	59768.1199	11 × 4 × 11	3180	-0.04 ± 0.27	-15.46 ± 0.04	0.18 ± 0.06	0.523 ± 0.002	0.89 ± 0.01	7
2022-07-08	59769.1235	12 × 4 × 11	3520	0.13 ± 0.26	-13.84 ± 0.04	1.80 ± 0.05	0.776 ± 0.002	0.90 ± 0.01	7
2022-07-10	59771.0531	12 × 4 × 11	3730	0.19 ± 0.26	-17.46 ± 0.04	-1.82 ± 0.06	0.262 ± 0.002	0.92 ± 0.01	7
2022-07-11	59772.0497	12 × 4 × 11	2330	-0.16 ± 0.38	-15.58 ± 0.04	0.06 ± 0.05	0.513 ± 0.002	0.93 ± 0.01	7
2022-07-12	59773.1041	12 × 4 × 11	3890	-0.03 ± 0.23	-13.82 ± 0.03	1.82 ± 0.05	0.778 ± 0.002	0.94 ± 0.01	7
2022-07-14	59775.0434	12 × 4 × 11	3690	0.33 ± 0.25	-17.42 ± 0.04	-1.78 ± 0.05	0.266 ± 0.001	0.96 ± 0.01	7
2022-07-15	59776.0796	12 × 4 × 11	3210	0.34 ± 0.27	-15.37 ± 0.04	0.28 ± 0.06	0.527 ± 0.001	0.97 ± 0.01	7
2022-08-13	59805.0415	11 × 4 × 11	1250	-1.34 ± 0.72	-13.90 ± 0.04	1.78 ± 0.05	0.819 ± 0.001	0.26 ± 0.01	8
2022-08-14	59805.9626	11 × 4 × 11	2890	-1.24 ± 0.29	-16.28 ± 0.04	-0.60 ± 0.05	0.051 ± 0.001	0.27 ± 0.01	8
2022-09-09	59832.1341	11 × 4 × 11	2780	-2.86 ± 0.33	-14.39 ± 0.04	1.33 ± 0.05	0.640 ± 0.001	0.53 ± 0.01	8
2022-09-12	59834.9742	11 × 4 × 11	2880	-2.62 ± 0.31	-17.10 ± 0.05	-1.38 ± 0.06	0.355 ± 0.001	0.56 ± 0.01	8
2022-09-14	59837.0139	11 × 4 × 11	3220	-2.14 ± 0.28	-14.33 ± 0.04	1.39 ± 0.05	0.868 ± 0.001	0.58 ± 0.01	8
2022-09-15	59837.9894	11 × 4 × 11	2550	-2.27 ± 0.34	-16.95 ± 0.04	-1.23 ± 0.05	0.114 ± 0.001	0.59 ± 0.01	8
2022-10-07	59860.0585	11 × 4 × 11	3660	-0.71 ± 0.25	-14.12 ± 0.04	1.63 ± 0.05	0.670 ± 0.001	0.81 ± 0.01	8
2022-10-15	59868.1379	11 × 4 × 11	3890	0.27 ± 0.25	-14.04 ± 0.03	1.72 ± 0.05	0.704 ± 0.001	0.89 ± 0.01	8
2022-10-19	59871.9739	11 × 4 × 11	3520	0.20 ± 0.25	-14.25 ± 0.04	1.51 ± 0.05	0.670 ± 0.001	0.93 ± 0.01	8
2023-06-24	60120.0910	11 × 4 × 11	3280	-2.27 ± 0.29	-17.45 ± 0.04	-1.41 ± 0.05	0.137 ± 0.001	0.40 ± 0.01	11
2023-07-08	60134.0471	11 × 4 × 11	3540	-2.56 ± 0.25	-14.53 ± 0.03	1.53 ± 0.05	0.651 ± 0.001	0.54 ± 0.01	11
2023-10-20	60237.9519	10 × 4 × 11	2500	-2.87 ± 0.36	-14.36 ± 0.03	1.80 ± 0.05	0.810 ± 0.001	0.58 ± 0.01	12
2023-10-26	60243.8551	11 × 4 × 11	2700	-2.09 ± 0.34	-17.91 ± 0.04	-1.74 ± 0.05	0.296 ± 0.001	0.64 ± 0.01	12
2023-12-04	60282.7335	11 × 4 × 11	3000	0.67 ± 0.29	-17.25 ± 0.04	-1.04 ± 0.05	0.085 ± 0.001	0.03 ± 0.01	13
2024-01-01	60310.8111	11 × 4 × 11	3650	-1.69 ± 0.27	-17.85 ± 0.04	-1.61 ± 0.05	0.154 ± 0.001	0.31 ± 0.01	13
2024-01-06	60315.7430	10 × 4 × 11	2390	-2.27 ± 0.38	-17.41 ± 0.04	-1.17 ± 0.05	0.395 ± 0.001	0.36 ± 0.01	13
2025-01-16	60691.9370	10 × 4 × 11	2920	0.33 ± 0.31	-17.92 ± 0.04	-1.33 ± 0.05	0.107 ± 0.002	0.11 ± 0.01	17
2025-08-09	60897.0520	10 × 4 × 11	2160	-0.10 ± 0.40	-14.52 ± 0.04	2.24 ± 0.05	0.748 ± 0.002	0.15 ± 0.02	19
2025-08-11	60899.0570	11 × 4 × 11	1900	0.24 ± 0.46	-18.61 ± 0.04	-1.85 ± 0.05	0.253 ± 0.002	0.17 ± 0.02	19
2025-12-06	61015.9453	10 × 4 × 11	2660	-2.23 ± 0.32	-15.02 ± 0.03	1.83 ± 0.04	0.681 ± 0.003	0.34 ± 0.02	20
2025-12-09	61018.8354	11 × 4 × 11	2980	-2.33 ± 0.29	-18.09 ± 0.04	-1.24 ± 0.05	0.409 ± 0.003	0.37 ± 0.02	20
2025-12-10	61019.9171	11 × 4 × 11	2830	-2.45 ± 0.31	-15.05 ± 0.03	1.80 ± 0.04	0.681 ± 0.003	0.38 ± 0.02	20

B. MCMC ANALYSIS

We performed an MCMC analysis using the `emcee` Python package (D. Foreman-Mackey et al. 2013) to estimate the parameters and associated uncertainties for Eq. 2 fit to the $RV_{\text{cog}} - RV_{\text{orb}}$ values (Sec. 5.1) and Eq. 6 fit to the $\langle B_z \rangle$ measurements (Sec. 5.2). We adopt uniform priors for all parameters, which are provided in Tables B2 and B3. For both Eqs. 2 and 6, the prior for the epoch t_0 was constrained to be near the midpoint of the observations ($t_{\text{mid}} = 2460097.3517$ HJD). We performed the sampling with the default ‘stretch move’ ensemble method (J. Goodman & J. Weare 2010) using 100 walkers and 10^5 steps. We verified convergence by ensuring that the chain length was greater than 50 times the autocorrelation time. The first 1000 steps were then discarded, and the chains were thinned by a factor of 100 to reduce correlations.

Figures B4 and B5, and show the marginalized posterior distributions plotted with the `corner` Python package (D. Foreman-Mackey 2016). The parameter values reported in Tables B2 and B3 are the median of the marginalized posterior distributions, and the associated 1σ uncertainties are the 16th and 84th percentiles.

Table B2. Model priors and posterior estimates for fit to $RV_{\text{cog}} - RV_{\text{orb}}$.

Parameter	Prior	Value
C [km s^{-1}]	$\mathcal{U}(-2, 0)$	$-1.247^{+0.008}_{-0.008}$
A [km s^{-1}]	$\mathcal{U}(-3, 0)$	$-1.87^{+0.01}_{-0.01}$
P_{puls} [d]	$\mathcal{U}(3.969, 3.975)$	$3.97197^{+0.00004}_{-0.00004}$
t_0 [HJD - 2460000]	$\mathcal{U}(95.50, 95.90)$	$95.715^{+0.005}_{-0.005}$

Table B3. Model priors and posterior estimates for fit to $\langle B_z \rangle$.

Parameter	Prior	Value
B_0 [G]	$\mathcal{U}(-3, 1)$	$-1.15^{+0.06}_{-0.06}$
B_1 [G]	$\mathcal{U}(0, 4)$	$1.52^{+0.06}_{-0.05}$
P_{rot} [d]	$\mathcal{U}(95, 105)$	$100.29^{+0.19}_{-0.19}$
t_0 [HJD - 2460000]	$\mathcal{U}(t_{\text{mid}} \pm \frac{1}{2}P_{\text{rot}})$	$79.59^{+0.83}_{-0.83}$

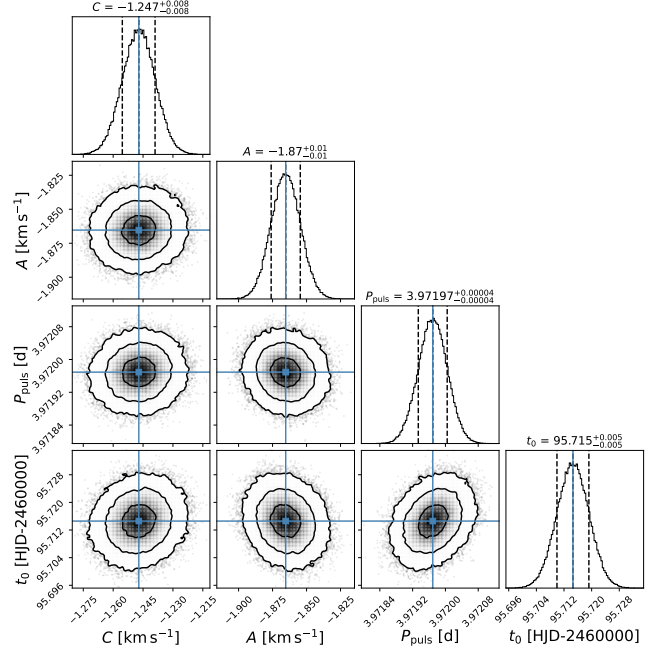


Figure B4. Marginalized posterior distributions inferred from fitting the $RV_{\text{cog}} - RV_{\text{orb}}$ measurements. The solid blue lines denote the median values and the dashed lines correspond to the 1σ credible range. The 2D contours correspond to the 1σ , 2σ and 3σ joint credible regions.

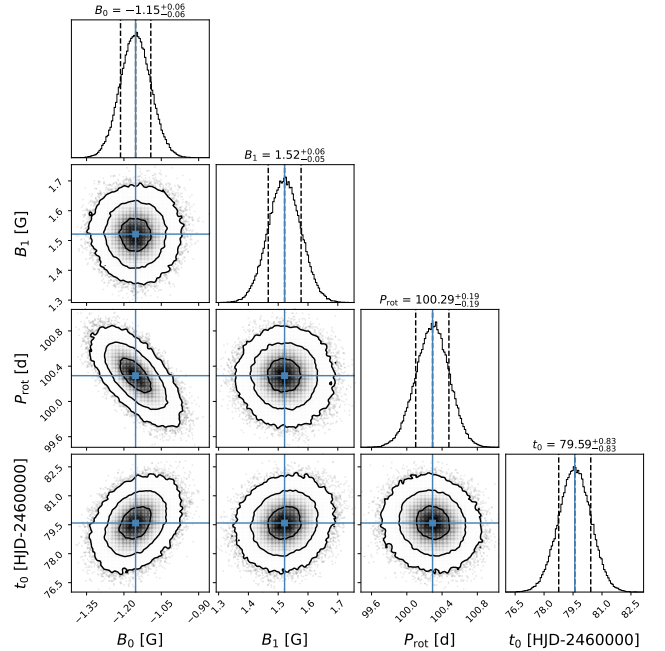


Figure B5. Marginalized posterior distributions inferred from fitting the $\langle B_z \rangle$ measurements. The solid blue lines denote the median values and the dashed lines correspond to the 1σ credible range. The 2D contours correspond to the 1σ , 2σ and 3σ joint credible regions.

REFERENCES

- Aerts, C., Simón-Díaz, S., Catala, C., et al. 2013, *A&A*, 557, A114, doi: [10.1051/0004-6361/201322097](https://doi.org/10.1051/0004-6361/201322097)
- Alecian, E., Wade, G. A., Catala, C., et al. 2013, *MNRAS*, 429, 1001, doi: [10.1093/mnras/sts383](https://doi.org/10.1093/mnras/sts383)
- Amard, L., Brun, A. S., & Palacios, A. 2024, *ApJ*, 974, 311, doi: [10.3847/1538-4357/ad6cd0](https://doi.org/10.3847/1538-4357/ad6cd0)
- Anderson, R. I. 2018, *A&A*, 611, L7, doi: [10.1051/0004-6361/201832585](https://doi.org/10.1051/0004-6361/201832585)
- Anderson, R. I. 2019, *A&A*, 623, A146, doi: [10.1051/0004-6361/201834703](https://doi.org/10.1051/0004-6361/201834703)
- Anderson, R. I., Ekström, S., Georgy, C., et al. 2014, *A&A*, 564, A100, doi: [10.1051/0004-6361/201322988](https://doi.org/10.1051/0004-6361/201322988)
- Anderson, R. I., Saio, H., Ekström, S., Georgy, C., & Meynet, G. 2016, *A&A*, 591, A8, doi: [10.1051/0004-6361/201528031](https://doi.org/10.1051/0004-6361/201528031)
- Anderson, R. I., Viviani, G., Shetye, S. S., et al. 2024, *A&A*, 686, A177, doi: [10.1051/0004-6361/202348400](https://doi.org/10.1051/0004-6361/202348400)
- Arellano Ferro, A. 1983, *ApJ*, 274, 755, doi: [10.1086/161486](https://doi.org/10.1086/161486)
- Astropy Collaboration, Price-Whelan, A. M., Lim, P. L., et al. 2022, *ApJ*, 935, 167, doi: [10.3847/1538-4357/ac7c74](https://doi.org/10.3847/1538-4357/ac7c74)
- Aurière, M., Wade, G. A., Konstantinova-Antova, R., et al. 2009, *A&A*, 504, 231, doi: [10.1051/0004-6361/200912050](https://doi.org/10.1051/0004-6361/200912050)
- Aurière, M., Konstantinova-Antova, R., Charbonnel, C., et al. 2015, *A&A*, 574, A90, doi: [10.1051/0004-6361/201424579](https://doi.org/10.1051/0004-6361/201424579)
- Baluev, R. V. 2008, *MNRAS*, 385, 1279, doi: [10.1111/j.1365-2966.2008.12689.x](https://doi.org/10.1111/j.1365-2966.2008.12689.x)
- Bang, T.-Y., Lee, B.-C., Choi, Y.-H., Han, I., & Park, M.-G. 2025, *ApJ*, 985, 176, doi: [10.3847/1538-4357/adcc13](https://doi.org/10.3847/1538-4357/adcc13)
- Barbey, K., Anderson, R. I., Viviani, G., et al. 2025, *A&A*, 698, A287, doi: [10.1051/0004-6361/202453395](https://doi.org/10.1051/0004-6361/202453395)
- Barron, J. A., Wade, G. A., Evans, N. R., Folsom, C. P., & Neilson, H. R. 2022, *MNRAS*, 512, 4021, doi: [10.1093/mnras/stac565](https://doi.org/10.1093/mnras/stac565)
- Barron, J. A., Wade, G. A., Folsom, C. P., & Kochukhov, O. 2024, in *IAU Symposium*, Vol. 361, *Massive Stars Near and Far*, ed. J. Mackey, J. S. Vink, & N. St-Louis, 233–235, doi: [10.1017/S1743921322002174](https://doi.org/10.1017/S1743921322002174)
- Bellinger, E. P., de Mink, S. E., van Rossem, W. E., & Justham, S. 2024, *ApJL*, 967, L39, doi: [10.3847/2041-8213/ad4990](https://doi.org/10.3847/2041-8213/ad4990)
- Bellot Rubio, L., & Orozco Suárez, D. 2019, *Living Reviews in Solar Physics*, 16, 1, doi: [10.1007/s41116-018-0017-1](https://doi.org/10.1007/s41116-018-0017-1)
- Bellotti, S., Petit, P., Jeffers, S. V., et al. 2025, *A&A*, 693, A269, doi: [10.1051/0004-6361/202452378](https://doi.org/10.1051/0004-6361/202452378)
- Bersier, D., & Burki, G. 1996, *A&A*, 306, 417
- Blazère, A., Petit, P., Lignières, F., et al. 2016, *A&A*, 586, A97, doi: [10.1051/0004-6361/201527556](https://doi.org/10.1051/0004-6361/201527556)
- Bond, H. E., Nelan, E. P., Remage Evans, N., Schaefer, G. H., & Harmer, D. 2018, *ApJ*, 853, 55, doi: [10.3847/1538-4357/aaa3f9](https://doi.org/10.3847/1538-4357/aaa3f9)
- Bono, G., Marconi, M., & Stellingwerf, R. F. 1999, *ApJS*, 122, 167, doi: [10.1086/313207](https://doi.org/10.1086/313207)
- Borisova, A., Aurière, M., Petit, P., et al. 2016, *A&A*, 591, A57, doi: [10.1051/0004-6361/201526726](https://doi.org/10.1051/0004-6361/201526726)
- Bruntt, H., Evans, N. R., Stello, D., et al. 2008, *ApJ*, 683, 433, doi: [10.1086/589565](https://doi.org/10.1086/589565)
- Buecke, R. 2021, *BAV Magazine Spectroscopy*, 9, 43
- Bugnet, L., Prat, V., Mathis, S., et al. 2021, *A&A*, 650, A53, doi: [10.1051/0004-6361/202039159](https://doi.org/10.1051/0004-6361/202039159)
- Campbell, W. W. 1899, *ApJ*, 10, 180, doi: [10.1086/140627](https://doi.org/10.1086/140627)
- Cantiello, M., & Braithwaite, J. 2019, *ApJ*, 883, 106, doi: [10.3847/1538-4357/ab3924](https://doi.org/10.3847/1538-4357/ab3924)
- Castelli, F., & Kurucz, R. L. 2003, in *Modelling of Stellar Atmospheres*, ed. N. Piskunov, W. W. Weiss, & D. F. Gray, Vol. 210, A20, doi: [10.48550/arXiv.astro-ph/0405087](https://doi.org/10.48550/arXiv.astro-ph/0405087)
- Charbonnel, C., Decressin, T., Lagarde, N., et al. 2017, *A&A*, 605, A102, doi: [10.1051/0004-6361/201526724](https://doi.org/10.1051/0004-6361/201526724)
- Dinshaw, N., Matthews, J. M., Walker, G. A. H., & Hill, G. M. 1989, *AJ*, 98, 2249, doi: [10.1086/115294](https://doi.org/10.1086/115294)
- Donati, J.-F., Catala, C., Landstreet, J. D., & Petit, P. 2006, in *Astronomical Society of the Pacific Conference Series*, Vol. 358, *Solar Polarization 4*, ed. R. Casini & B. W. Lites, 362
- Donati, J.-F., & Landstreet, J. D. 2009, *ARA&A*, 47, 333, doi: [10.1146/annurev-astro-082708-101833](https://doi.org/10.1146/annurev-astro-082708-101833)
- Donati, J. F., Semel, M., Carter, B. D., Rees, D. E., & Collier Cameron, A. 1997, *MNRAS*, 291, 658, doi: [10.1093/mnras/291.4.658](https://doi.org/10.1093/mnras/291.4.658)
- Donati, J. F., Semel, M., & Rees, D. E. 1992, *A&A*, 265, 669
- Donati, J.-F., Lehmann, L. T., Cristofari, P. I., et al. 2023, *MNRAS*, 525, 2015, doi: [10.1093/mnras/stad2301](https://doi.org/10.1093/mnras/stad2301)
- Ekström, S., Meynet, G., Maeder, A., & Barblan, F. 2008, *A&A*, 478, 467, doi: [10.1051/0004-6361:20078095](https://doi.org/10.1051/0004-6361:20078095)
- Ekström, S., Georgy, C., Eggenberger, P., et al. 2012, *A&A*, 537, A146, doi: [10.1051/0004-6361/201117751](https://doi.org/10.1051/0004-6361/201117751)
- Engle, S. 2015, PhD thesis, James Cook University, Australia
- Engle, S. G., Guinan, E. F., & Harmanec, P. 2018, *Research Notes of the American Astronomical Society*, 2, 126, doi: [10.3847/2515-5172/aad2d0](https://doi.org/10.3847/2515-5172/aad2d0)
- Evans, N. R., Guinan, E., Engle, S., et al. 2010, *AJ*, 139, 1968, doi: [10.1088/0004-6256/139/5/1968](https://doi.org/10.1088/0004-6256/139/5/1968)
- Evans, N. R., Sasselov, D. D., & Short, C. I. 2002, *ApJ*, 567, 1121, doi: [10.1086/338583](https://doi.org/10.1086/338583)

- Evans, N. R., Schaefer, G. H., Bond, H. E., et al. 2008, *AJ*, 136, 1137, doi: [10.1088/0004-6256/136/3/1137](https://doi.org/10.1088/0004-6256/136/3/1137)
- Evans, N. R., Karovska, M., Bond, H. E., et al. 2018, *ApJ*, 863, 187, doi: [10.3847/1538-4357/aad410](https://doi.org/10.3847/1538-4357/aad410)
- Evans, N. R., Engle, S., Pillitteri, I., et al. 2022, *ApJ*, 938, 153, doi: [10.3847/1538-4357/ac6fdf](https://doi.org/10.3847/1538-4357/ac6fdf)
- Evans, N. R., Schaefer, G. H., Gallenne, A., et al. 2024, *ApJ*, 971, 190, doi: [10.3847/1538-4357/ad5e7a](https://doi.org/10.3847/1538-4357/ad5e7a)
- Fadeyev, Y. A. 2015, *MNRAS*, 449, 1011, doi: [10.1093/mnras/stv412](https://doi.org/10.1093/mnras/stv412)
- Feast, M. W., & Catchpole, R. M. 1997, *MNRAS*, 286, L1, doi: [10.1093/mnras/286.L1](https://doi.org/10.1093/mnras/286.L1)
- Ferraro, F. R., Mucciarelli, A., Lanzoni, B., et al. 2023, *Nature Communications*, 14, 2584, doi: [10.1038/s41467-023-38153-w](https://doi.org/10.1038/s41467-023-38153-w)
- Folsom, C. P. 2018, *Contributions of the Astronomical Observatory Skalnaté Pleso*, 48, 53
- Folsom, C. P., Bagnulo, S., Wade, G. A., et al. 2012, *MNRAS*, 422, 2072, doi: [10.1111/j.1365-2966.2012.20718.x](https://doi.org/10.1111/j.1365-2966.2012.20718.x)
- Folsom, C. P., Petit, P., Bouvier, J., et al. 2016, *MNRAS*, 457, 580, doi: [10.1093/mnras/stv2924](https://doi.org/10.1093/mnras/stv2924)
- Folsom, C. P., Bouvier, J., Petit, P., et al. 2018, *MNRAS*, 474, 4956, doi: [10.1093/mnras/stx3021](https://doi.org/10.1093/mnras/stx3021)
- Folsom, C. P., Erba, C., Petit, V., et al. 2025, *Journal of Open Source Software*, 10, 7891, doi: [10.21105/joss.07891](https://doi.org/10.21105/joss.07891)
- Foreman-Mackey, D. 2016, *The Journal of Open Source Software*, 1, 24, doi: [10.21105/joss.00024](https://doi.org/10.21105/joss.00024)
- Foreman-Mackey, D., Hogg, D. W., Lang, D., & Goodman, J. 2013, *PASP*, 125, 306, doi: [10.1086/670067](https://doi.org/10.1086/670067)
- Fossati, L., Castro, N., Schöller, M., et al. 2015, *A&A*, 582, A45, doi: [10.1051/0004-6361/201526725](https://doi.org/10.1051/0004-6361/201526725)
- Frost, A. J., Sana, H., Mahy, L., et al. 2024, *Science*, 384, 214, doi: [10.1126/science.adg7700](https://doi.org/10.1126/science.adg7700)
- Fuller, J., Cantiello, M., Stello, D., Garcia, R. A., & Bildsten, L. 2015, *Science*, 350, 423, doi: [10.1126/science.aac6933](https://doi.org/10.1126/science.aac6933)
- Georgiev, S., Lèbre, A., Josselin, E., et al. 2023, *MNRAS*, 522, 3861, doi: [10.1093/mnras/stad1210](https://doi.org/10.1093/mnras/stad1210)
- Georgy, C., Ekström, S., Eggenberger, P., et al. 2013, *A&A*, 558, A103, doi: [10.1051/0004-6361/201322178](https://doi.org/10.1051/0004-6361/201322178)
- Gillet, D., Fokin, A. B., Breitfellner, M. G., Mazauric, S., & Nicolas, A. 1999, *A&A*, 344, 935
- Goodman, J., & Weare, J. 2010, *Communications in Applied Mathematics and Computational Science*, 5, 65, doi: [10.2140/camcos.2010.5.65](https://doi.org/10.2140/camcos.2010.5.65)
- Gray, D. F. 1975, *ApJ*, 202, 148, doi: [10.1086/153960](https://doi.org/10.1086/153960)
- Gray, D. F. 1982, *ApJ*, 255, 200, doi: [10.1086/159818](https://doi.org/10.1086/159818)
- Gray, D. F. 2022, *The Observation and Analysis of Stellar Photospheres*, 4th edn. (Cambridge: Cambridge University Press)
- Gray, D. F., & Stevenson, K. B. 2007, *PASP*, 119, 398, doi: [10.1086/518128](https://doi.org/10.1086/518128)
- Grunhut, J. H., Wade, G. A., Hanes, D. A., & Alecian, E. 2010, *MNRAS*, 408, 2290, doi: [10.1111/j.1365-2966.2010.17275.x](https://doi.org/10.1111/j.1365-2966.2010.17275.x)
- Grunhut, J. H., Wade, G. A., Neiner, C., et al. 2017, *MNRAS*, 465, 2432, doi: [10.1093/mnras/stw2743](https://doi.org/10.1093/mnras/stw2743)
- Harris, C. R., Millman, K. J., van der Walt, S. J., et al. 2020, *Nature*, 585, 357, doi: [10.1038/s41586-020-2649-2](https://doi.org/10.1038/s41586-020-2649-2)
- Hatzes, A. P., & Cochran, W. D. 1995, *ApJ*, 452, 401, doi: [10.1086/176311](https://doi.org/10.1086/176311)
- Hatzes, A. P., & Cochran, W. D. 2000, *AJ*, 120, 979, doi: [10.1086/301502](https://doi.org/10.1086/301502)
- Henneco, J., Schneider, F. R. N., Hekker, S., & Aerts, C. 2024, *A&A*, 690, A65, doi: [10.1051/0004-6361/202450508](https://doi.org/10.1051/0004-6361/202450508)
- Hertzsprung, E. 1911, *Astronomische Nachrichten*, 189, 89, doi: [10.1002/asna.19111890602](https://doi.org/10.1002/asna.19111890602)
- Hilditch, R. W. 2001, *An Introduction to Close Binary Stars* (Cambridge University Press)
- Hocdé, V., Moskalik, P., Gorynya, N. A., et al. 2024, *A&A*, 689, A224, doi: [10.1051/0004-6361/202347798](https://doi.org/10.1051/0004-6361/202347798)
- Hocdé, V., Nardetto, N., Lagadec, E., et al. 2020, *A&A*, 633, A47, doi: [10.1051/0004-6361/201935848](https://doi.org/10.1051/0004-6361/201935848)
- Hunter, J. D. 2007, *Computing in Science & Engineering*, 9, 90, doi: [10.1109/MCSE.2007.55](https://doi.org/10.1109/MCSE.2007.55)
- Jermyn, A. S., Anders, E. H., Lecoanet, D., & Cantiello, M. 2022, *ApJS*, 262, 19, doi: [10.3847/1538-4365/ac7cee](https://doi.org/10.3847/1538-4365/ac7cee)
- Käpylä, P. J., Browning, M. K., Brun, A. S., Guerrero, G., & Warnecke, J. 2023, *SSRv*, 219, 58, doi: [10.1007/s11214-023-01005-6](https://doi.org/10.1007/s11214-023-01005-6)
- Kienzle, F., Moskalik, P., Bersier, D., & Pont, F. 1999, *A&A*, 341, 818
- Kochukhov, O. 2016, in *Lecture Notes in Physics*, Berlin Springer Verlag, ed. J.-P. Rozelot & C. Neiner, Vol. 914 (Springer), 177, doi: [10.1007/978-3-319-24151-7_9](https://doi.org/10.1007/978-3-319-24151-7_9)
- Kochukhov, O., Makaganiuk, V., & Piskunov, N. 2010, *A&A*, 524, A5, doi: [10.1051/0004-6361/201015429](https://doi.org/10.1051/0004-6361/201015429)
- Korčáková, D., Sestito, F., Manset, N., et al. 2022, *A&A*, 659, A35, doi: [10.1051/0004-6361/202141016](https://doi.org/10.1051/0004-6361/202141016)
- Korčáková, D., Dvořáková, N., Bermejo Lozano, I., et al. 2025, *Galaxies*, 13, 46, doi: [10.3390/galaxies13030046](https://doi.org/10.3390/galaxies13030046)
- Kovtyukh, V. V., & Gorlova, N. I. 2000, *A&A*, 358, 587
- Kupka, F., Ballot, J., & Muthsam, H. J. 2009, *Communications in Asteroseismology*, 160, 30, doi: [10.48550/arXiv.0905.0070](https://doi.org/10.48550/arXiv.0905.0070)
- Kurucz, R. 1993, *Robert Kurucz CD-ROM*, 13
- Kurucz, R. L. 1970, *SAO Special Report*, 309

- Landstreet, J. D. 1988, *ApJ*, 326, 967, doi: [10.1086/166155](https://doi.org/10.1086/166155)
- Lavail, A., López Ariste, A., Pilate, Q., et al. 2025, *Research Notes of the American Astronomical Society*, 9, 327, doi: [10.3847/2515-5172/ae290e](https://doi.org/10.3847/2515-5172/ae290e)
- Lèbre, A., Aurière, M., Fabas, N., et al. 2014, *A&A*, 561, A85, doi: [10.1051/0004-6361/201322826](https://doi.org/10.1051/0004-6361/201322826)
- Lee, B.-C., Han, I., Park, M.-G., Kim, K.-M., & Mkrtichian, D. E. 2012, *A&A*, 543, A37, doi: [10.1051/0004-6361/201118539](https://doi.org/10.1051/0004-6361/201118539)
- Lee, B.-C., Mkrtichian, D. E., Han, I., Park, M.-G., & Kim, K.-M. 2008, *AJ*, 135, 2240, doi: [10.1088/0004-6256/135/6/2240](https://doi.org/10.1088/0004-6256/135/6/2240)
- Lomb, N. R. 1976, *Ap&SS*, 39, 447, doi: [10.1007/BF00648343](https://doi.org/10.1007/BF00648343)
- López Ariste, A. 2002, *ApJ*, 564, 379, doi: [10.1086/324215](https://doi.org/10.1086/324215)
- Martin, A. J., Neiner, C., Oksala, M. E., et al. 2018, *MNRAS*, 475, 1521, doi: [10.1093/mnras/stx3264](https://doi.org/10.1093/mnras/stx3264)
- Martínez González, M. J., Collados, M., Ruiz Cobo, B., & Beck, C. 2008, *A&A*, 477, 953, doi: [10.1051/0004-6361:20078506](https://doi.org/10.1051/0004-6361:20078506)
- Mérand, A., Kervella, P., Coudé du Foresto, V., et al. 2006, *A&A*, 453, 155, doi: [10.1051/0004-6361:20054466](https://doi.org/10.1051/0004-6361:20054466)
- Meynet, G., & Maeder, A. 2000, *A&A*, 361, 101, doi: [10.48550/arXiv.astro-ph/0006404](https://doi.org/10.48550/arXiv.astro-ph/0006404)
- Morel, T., Castro, N., Fossati, L., et al. 2015, in *IAU Symposium*, Vol. 307, *New Windows on Massive Stars*, ed. G. Meynet, C. Georgy, J. Groh, & P. Stee, 342–347, doi: [10.1017/S1743921314007054](https://doi.org/10.1017/S1743921314007054)
- Moskalik, P., & Gorynya, N. A. 2005, *AcA*, 55, 247, doi: [10.48550/arXiv.astro-ph/0507076](https://doi.org/10.48550/arXiv.astro-ph/0507076)
- Neilson, H. R. 2014, *A&A*, 563, A48, doi: [10.1051/0004-6361/201423482](https://doi.org/10.1051/0004-6361/201423482)
- Neilson, H. R., Engle, S. G., Guinan, E., et al. 2012, *ApJL*, 745, L32, doi: [10.1088/2041-8205/745/2/L32](https://doi.org/10.1088/2041-8205/745/2/L32)
- Neiner, C., Mathis, S., Alecian, E., et al. 2015, in *IAU Symposium*, Vol. 305, *Polarimetry*, ed. K. N. Nagendra, S. Bagnulo, R. Centeno, & M. Jesús Martínez González, 61–66, doi: [10.1017/S1743921315004524](https://doi.org/10.1017/S1743921315004524)
- Neiner, C., Oksala, M. E., Georgy, C., et al. 2017, *MNRAS*, 471, 1926, doi: [10.1093/mnras/stx1549](https://doi.org/10.1093/mnras/stx1549)
- Oksala, M. E., Wade, G. A., Townsend, R. H. D., et al. 2012, *MNRAS*, 419, 959, doi: [10.1111/j.1365-2966.2011.19753.x](https://doi.org/10.1111/j.1365-2966.2011.19753.x)
- Peterson, R. C., Carney, B. W., & Latham, D. W. 1996, *ApJL*, 465, L47, doi: [10.1086/310134](https://doi.org/10.1086/310134)
- Petit, P., Lignières, F., Aurière, M., et al. 2011, *A&A*, 532, L13, doi: [10.1051/0004-6361/201117573](https://doi.org/10.1051/0004-6361/201117573)
- Petit, V., Wade, G. A., Schneider, F. R. N., et al. 2019, *MNRAS*, 489, 5669, doi: [10.1093/mnras/stz2469](https://doi.org/10.1093/mnras/stz2469)
- Press, W. H., Teukolsky, S. A., Vetterling, W. T., & Flannery, B. P. 1992, *Numerical recipes in FORTRAN. The art of scientific computing* (Cambridge University Press)
- Preston, G. W., Sneden, C., Chadid, M., Thompson, I. B., & Shtetman, S. A. 2019, *AJ*, 157, 153, doi: [10.3847/1538-3881/ab0ae1](https://doi.org/10.3847/1538-3881/ab0ae1)
- Queloz, D., Henry, G. W., Sivan, J. P., et al. 2001, *A&A*, 379, 279, doi: [10.1051/0004-6361:20011308](https://doi.org/10.1051/0004-6361:20011308)
- Ripepi, V., Catanzaro, G., Molnár, L., et al. 2021, *A&A*, 647, A111, doi: [10.1051/0004-6361/202040123](https://doi.org/10.1051/0004-6361/202040123)
- Roemer, E. 1965, *ApJ*, 141, 1415, doi: [10.1086/148230](https://doi.org/10.1086/148230)
- Sabin, L., Wade, G. A., & Lèbre, A. 2015, *MNRAS*, 446, 1988, doi: [10.1093/mnras/stu2227](https://doi.org/10.1093/mnras/stu2227)
- Scargle, J. D. 1982, *ApJ*, 263, 835, doi: [10.1086/160554](https://doi.org/10.1086/160554)
- Schneider, F. R. N. 2025, arXiv e-prints, arXiv:2509.18421, doi: [10.48550/arXiv.2509.18421](https://doi.org/10.48550/arXiv.2509.18421)
- Schneider, F. R. N., Ohlmann, S. T., Podsiadlowski, P., et al. 2019, *Nature*, 574, 211, doi: [10.1038/s41586-019-1621-5](https://doi.org/10.1038/s41586-019-1621-5)
- Schneider, F. R. N., Podsiadlowski, P., Langer, N., Castro, N., & Fossati, L. 2016, *MNRAS*, 457, 2355, doi: [10.1093/mnras/stw148](https://doi.org/10.1093/mnras/stw148)
- Seidel, L. 1852, *IJK1*, *Dokl. Akad. Wiss. Munchen*, 6, 564
- Shenar, T., Wade, G. A., Marchant, P., et al. 2023, *Science*, 381, 761, doi: [10.1126/science.ade3293](https://doi.org/10.1126/science.ade3293)
- Shultz, M., Wade, G. A., Petit, V., et al. 2014, *MNRAS*, 438, 1114, doi: [10.1093/mnras/stt2260](https://doi.org/10.1093/mnras/stt2260)
- Shultz, M. E., Wade, G. A., Rivinius, T., et al. 2018, *MNRAS*, 475, 5144, doi: [10.1093/mnras/sty103](https://doi.org/10.1093/mnras/sty103)
- Sikora, J., Wade, G. A., Power, J., & Neiner, C. 2019a, *MNRAS*, 483, 2300, doi: [10.1093/mnras/sty3105](https://doi.org/10.1093/mnras/sty3105)
- Sikora, J., Wade, G. A., Power, J., & Neiner, C. 2019b, *MNRAS*, 483, 3127, doi: [10.1093/mnras/sty2895](https://doi.org/10.1093/mnras/sty2895)
- Silvester, J., Kochukhov, O., & Wade, G. A. 2014, *MNRAS*, 440, 182, doi: [10.1093/mnras/stu306](https://doi.org/10.1093/mnras/stu306)
- Stepien, K. 1993, *ApJ*, 416, 368, doi: [10.1086/173240](https://doi.org/10.1086/173240)
- Storm, J., Gieren, W., Fouqué, P., et al. 2011, *A&A*, 534, A94, doi: [10.1051/0004-6361/201117155](https://doi.org/10.1051/0004-6361/201117155)
- Stothers, R. B. 2009, *ApJL*, 696, L37, doi: [10.1088/0004-637X/696/1/L37](https://doi.org/10.1088/0004-637X/696/1/L37)
- Stuck, M., Pratt, J., Baraffe, I., et al. 2025, *A&A*, 698, A304, doi: [10.1051/0004-6361/202555172](https://doi.org/10.1051/0004-6361/202555172)
- Torres, G. 2023, *MNRAS*, 526, 2510, doi: [10.1093/mnras/stad2735](https://doi.org/10.1093/mnras/stad2735)
- Trahin, B., Breuval, L., Kervella, P., et al. 2021, *A&A*, 656, A102, doi: [10.1051/0004-6361/202141680](https://doi.org/10.1051/0004-6361/202141680)
- Tsvetkova, S., Petit, P., Konstantinova-Antova, R., et al. 2017, *A&A*, 599, A72, doi: [10.1051/0004-6361/201527034](https://doi.org/10.1051/0004-6361/201527034)

- Turner, D. G., Kovtyukh, V. V., Usenko, I. A., & Gorlova, N. I. 2013, *ApJL*, 762, L8,
doi: [10.1088/2041-8205/762/1/L8](https://doi.org/10.1088/2041-8205/762/1/L8)
- Turner, D. G., Savoy, J., Derrah, J., Abdel-Sabour Abdel-Latif, M., & Berdnikov, L. N. 2005, *PASP*, 117, 207, doi: [10.1086/427838](https://doi.org/10.1086/427838)
- ud-Doula, A., Owocki, S. P., & Townsend, R. H. D. 2009, *MNRAS*, 392, 1022,
doi: [10.1111/j.1365-2966.2008.14134.x](https://doi.org/10.1111/j.1365-2966.2008.14134.x)
- Usenko, I. A., & Klochkova, V. G. 2008, *MNRAS*, 387, L1,
doi: [10.1111/j.1745-3933.2008.00426.x](https://doi.org/10.1111/j.1745-3933.2008.00426.x)
- Usenko, I. A., Miroshnichenko, A. S., Danford, S., et al. 2024, *Odessa Astronomical Publications*, 37, 57,
doi: [10.18524/1810-4215.2024.37.314974](https://doi.org/10.18524/1810-4215.2024.37.314974)
- Usenko, I. A., Miroshnichenko, A. S., Klochkova, V. G., & Yushkin, M. V. 2005, *MNRAS*, 362, 1219,
doi: [10.1111/j.1365-2966.2005.09353.x](https://doi.org/10.1111/j.1365-2966.2005.09353.x)
- van Leeuwen, F. 2007, *A&A*, 474, 653,
doi: [10.1051/0004-6361:20078357](https://doi.org/10.1051/0004-6361:20078357)
- van Leeuwen, F. 2013, *A&A*, 550, L3,
doi: [10.1051/0004-6361/201220871](https://doi.org/10.1051/0004-6361/201220871)
- VanderPlas, J. T. 2018, *ApJS*, 236, 16,
doi: [10.3847/1538-4365/aab766](https://doi.org/10.3847/1538-4365/aab766)
- Verdugo, E., Talavera, A., Gómez de Castro, A. I., et al. 2003, in *Astronomical Society of the Pacific Conference Series*, Vol. 305, *Magnetic Fields in O, B and A Stars: Origin and Connection to Pulsation, Rotation and Mass Loss*, ed. L. A. Balona, H. F. Henrichs, & R. Medupe, 364
- Villebrun, F., Alecian, E., Hussain, G., et al. 2019, *A&A*, 622, A72, doi: [10.1051/0004-6361/201833545](https://doi.org/10.1051/0004-6361/201833545)
- Vynatheya, P., Ryu, T., Wang, C., Sills, A., & Pakmor, R. 2026, *ApJ*, 999, 64, doi: [10.3847/1538-4357/ae40ba](https://doi.org/10.3847/1538-4357/ae40ba)
- Wade, G. A., Bagnulo, S., Drouin, D., Landstreet, J. D., & Monin, D. 2007, *MNRAS*, 376, 1145,
doi: [10.1111/j.1365-2966.2007.11495.x](https://doi.org/10.1111/j.1365-2966.2007.11495.x)
- Wade, G. A., Bagnulo, S., Kochukhov, O., et al. 2001, *A&A*, 374, 265, doi: [10.1051/0004-6361:20010735](https://doi.org/10.1051/0004-6361:20010735)
- Wade, G. A., Donati, J.-F., Landstreet, J. D., & Shorlin, S. L. S. 2000, *MNRAS*, 313, 851,
doi: [10.1046/j.1365-8711.2000.03271.x](https://doi.org/10.1046/j.1365-8711.2000.03271.x)
- Wade, G. A., Oksala, M., Neiner, C., Boucher, É., & Barron, J. A. 2025, *ApJL*, 988, L38,
doi: [10.3847/2041-8213/ade9ac](https://doi.org/10.3847/2041-8213/ade9ac)
- Wade, G. A., Neiner, C., Alecian, E., et al. 2016, *MNRAS*, 456, 2, doi: [10.1093/mnras/stv2568](https://doi.org/10.1093/mnras/stv2568)
- Weber, E. J., & Davis, Jr., L. 1967, *ApJ*, 148, 217,
doi: [10.1086/149138](https://doi.org/10.1086/149138)
- Zechmeister, M., & Kürster, M. 2009, *A&A*, 496, 577,
doi: [10.1051/0004-6361:200811296](https://doi.org/10.1051/0004-6361:200811296)
- Zhao, L., Song, H., Meynet, G., et al. 2023, *A&A*, 674, A92, doi: [10.1051/0004-6361/202245665](https://doi.org/10.1051/0004-6361/202245665)